Seasonal dispersal of fjord meltwaters as an important source of iron and manganese to coastal Antarctic phytoplankton

Kiefer Forsch[1], Lisa Hahn-Woernle[2], Robert M. Sherrell[3], Vincent J. Roccanova[3], Kaixan Bu[3], David Burdige[4], Maria Vernet[1], Katherine A. Barbeau[1]

[1]Scripps Institution of Oceanography, University of California San Diego, La Jolla, 92037, USA
[2]Department of Oceanography, University of Hawai`i, Manoa, 96822, USA
[3]Departments of Marine and Coastal Sciences and Earth and Planetary Sciences, Rutgers University, New Brunswick, 08901, USA
[4]Department of Ocean & Earth Sciences, Old Dominion University, Norfolk, 23529, USA

Correspondence to: Kiefer O. Forsch (kforsch@ucsd.edu)

Abstract. Glacial meltwater from the western Antarctic Ice Sheet is hypothesized to be an important source of cryospheric iron, fertilizing the Southern Ocean, yet its trace metal composition and factors that control its dispersal remain poorly constrained. Here we characterize meltwater iron sources in a heavily glaciated western Antarctic Peninsula (WAP) fjord. Using dissolved and particulate ratios of manganese-to-iron in meltwaters, porewaters, and seawater, we show that surface glacial melt and subglacial plumes contribute to the seasonal cycle of iron and manganese within a fjord still relatively unaffected by climate change-induced glacial retreat. Organic ligands derived from the phytoplankton bloom and the glaciers bind dissolved iron and facilitate the solubilization of particulate iron downstream. Using a numerical model, we show that buoyant plumes generated by outflow from the subglacial hydrologic system, enriched in labile particulate trace metals derived from a chemically-modified crustal source, can supply iron to the fjord euphotic zone through vertical mixing, and that prolonged katabatic wind events enhance export of meltwater out of the fjord. Thus, we identify an important atmosphere-ice-ocean coupling intimately tied to coastal iron biogeochemistry and primary productivity along the WAP.

1 Introduction

Warm atmospheric temperatures are accelerating glacial retreat and increasing meltwater discharge, rapidly changing Earth's cryosphere (Rignot *et al.*, 2013; Mouginot *et al.*, 2019). Ranging from diffuse flows to waterfalls and streams, cryospheric meltwaters deliver dissolved and particulate material, altering coastal ocean biogeochemistry. Glacial meltwater enters the ocean through surface runoff, direct melting of glacial ice (including icebergs), and discharge from liquid water reservoirs beneath glaciers, carrying iron (Fe) and other trace metals weathered from continental crust. In the surface ocean, the delivery of new Fe is critical for the growth of phytoplankton; and when enhanced, naturally or artificially, primary production, and potentially carbon export, increase (Boyd *et al.*, 2019). However, direct measurements of Fe in heavily glaciated fjords reveal that up to 90-99% of dissolved Fe (dFe) originating from glaciers is removed upon mixing with seawater due to estuarine-type

removal processes, including: precipitation of insoluble oxyhydroxides, adsorption to the surfaces of particles, and aggregation of colloids and particles (Boyle, Edmond and Sholkovitz, 1977; Schroth *et al.*, 2014). Together, these processes are known as scavenging and constitute a major control on the distribution of Fe in the ocean by converting soluble forms of Fe into colloidal

35   aggregates and particles (Wu *et al.* 2001). Constraints on the flux of newly delivered glacial Fe that escapes this sink and is transported across continental shelves will enable better predictions of open ocean primary production and carbon sequestration, especially in oceanic regimes where Fe is a limiting nutrient. Given that recent studies revealed a critical role for manganese (Mn) in co-limiting primary production in coastal Antarctica and the core of the Antarctic Circumpolar Current (Wu *et al.*, 2019; Browning *et al.*, 2021), an investigation of Mn delivery by glacial meltwaters is also needed (Bown *et al.*,

40   2018). Currently, very little is known about how glacial meltwaters affect marine Mn cycling.

Evidence for Fe delivery from the cryosphere is historically based on geochemical analysis of endmember glacial discharge (Hawkings *et al.,* 2014; Raiswell and Canfield 2012; Hodson *et al.,* 2017; Hawkings *et al.,* 2020), and discrete sampling of glacial ice (e.g. Hopwood *et al.* 2018) and seawater adjacent to marine-terminating glaciers and ice sheets (Hopwood *et al.,* 2016; Annett *et al.,* 2015; Gerringa *et al.,* 2015; Alderkamp *et al.,* 2012; Sherrell *et al.,* 2018). Trace metal studies at the ice-

45   ocean interface have been conducted previously in fjords experiencing intense seasonal melt, such as in Alaska, Greenland, and Svalbard (Schroth *et al.*, 2014; Zhang *et al.*, 2015; Hopwood *et al.*, 2016; Kanna *et al.*, 2020). These temperate and high Arctic coastal waters are experiencing large freshwater and sediment fluxes as a result of increased glacial discharge, that in turn creates extreme physical and geochemical gradients. Ultimately, such dramatic changes in turbidity decrease light availability while strong stratification reduces macronutrient supply to local primary producers (Meire *et al.*, 2017; Holding *et*

50   *al.*, 2019). Even with high particulate and dissolved Fe contents, meltwaters from these fjords do not feed directly into offshore waters without undergoing significant scavenging, mixing and dilution (Hopwood *et al.*, 2015), bringing into question the effectiveness with which glacial meltwater-derived Fe may fertilize the surrounding ocean.

In Antarctica, fjords are less well-studied than their Arctic counterparts, but are also locations of intense seasonal blooms with comparable or higher primary production relative to the adjacent continental shelves, and high sequestration efficiencies of

55   organic carbon (Vernet *et al.*, 2008; Grange and Smith 2013; Taylor *et al.*, 2020). Along the western Antarctic Peninsula (WAP), 674 marine-terminating glaciers drain into the coastal ocean, primarily in fjords (Cook *et al.*, 2016). The vast majority of these marine-terminating glaciers are retreating due to intrusions of warm deep water from the shelf, but many still remain as 'cold-water' glaciers (that is, local ocean temperatures are too cold to melt the glacier terminus), particularly in the northern WAP where Weddell Water from the eastern side advects and mixes into the Bransfield Strait (Pritchard and Vaughan, 2007;

60   Cook *et al.*, 2016). These glaciers are thought to have relatively small subglacial meltwater discharge, with suspended sediment signatures that spread laterally in the coastal ocean (Domack and Ishman, 1993; Domack and Williams, 2011). This makes cold glacio-marine Antarctic fjords unique locations for sampling subglacial discharge with minimal dilution by ambient seawater.

Subglacial environments distinguish themselves from other cryospheric sources of Fe to the oceanic euphotic zone. Within the

65   subglacial cavity, anoxia develops due to enhanced microbial respiration processes, high weathering rates, and limited

diffusion of oxygen and exchange with the coastal ocean (Mikucki *et al.*, 2009). The result is increased solubility of iron as Fe(II), and other redox sensitive elements, such as Mn. Meltwater discharge from beneath marine-terminating glaciers enters the ocean in the subsurface but may be mixed into the surface because of the positive buoyancy of meltwater-seawater mixtures. Enhanced vertical shear occurs episodically in the Antarctic coastal ocean as cooled dense parcels of air accelerate down ice sheets, generating the strongest coastal winds on Earth (>30 m s^{-1}), near the coast. These episodic katabatic wind events could also be important for enhancing the supply of subsurface meltwaters to the surface (Jackson *et al.*, 2014; Lundesgaard *et al.*, 2019). The subglacial meltwater source represents a large uncertainty in the supply of cryospheric Fe to the ocean given the challenge of acquiring samples of this reservoir directly or with minimal alteration, particularly in Arctic environments with intense seasonal melt flows and associated sediment turbidity (Straneo and Cenedese, 2015).

We present trace metal results from two expeditions (December 2015 and April 2016) to Andvord Bay, a cold glacio-marine fjord located mid-latitude along the WAP. This study is part of the FjordEco project which assessed the ecosystem function and seasonality of Andvord Bay (Pan *et al.*, 2019; Pan *et al.*, 2020; Ziegler *et al.*, 2020; Eidam *et al.*, 2019; Lundesgaard *et al.*, 2020, 2019; Hahn-Woernle *et al.*, 2020). The WAP is host to the most extensive collection of glaciomarine fjords on the Antarctic continent, and its shelf waters are subject to ongoing biogeochemical and ecological alteration linked to large-scale changes to the western Antarctic Ice Sheet (Henley *et al.*, 2020). We present a detailed and unprecedented picture of fjord Fe and Mn biogeochemistry and seasonality in the early stages of glacier retreat associated with recent climate change (Pritchard and Vaughan, 2007).

2 Methods

2.1 Oceanographic setting and sampling

Andvord Bay is a glacio-marine fjord located mid-latitude along the west Antarctic Peninsula (WAP). This site was chosen because it has been identified as a productivity "hotspot" (Grange and Smith, 2013), and because of its proximity to long-standing ecological research programs (Palmer Long Term Ecological Research program). This location is characterized by converging deep water masses with distinct physical properties (relatively warm modified Upper Circumpolar Deep Water, cold Weddell Water). Bordering Andvord Bay are 11 marine-terminating glaciers (Fig. 1) with Moser and Bagshawe glaciers responsible for the majority of the solid ice flux. These glaciers are cold-water (-1 to -0.5 °C) resulting in weak meltwater signatures within the fjord (Lundesgaard *et al.*, 2020). Observations and sampling of Andvord Bay were conducted during two cruises as part of the FjordEco program: LMG15-10 from 27 November to 22 December 2015 (late Spring) on R/V *Laurence M. Gould*, NBP16-03 from 4 April to 26 April (Fall) aboard R/V *Nathaniel B. Palmer*. On December 11, 2015 a strong katabatic wind event, with peak along-fjord velocities of 30 m s^{-1}, was observed and lasted for 5 days. Atmospheric observations by two automatic weather stations (Neko Harbor, Useful Island) recorded episodes of high velocity katabatic winds between field seasons, showing that these are common events in this study region.
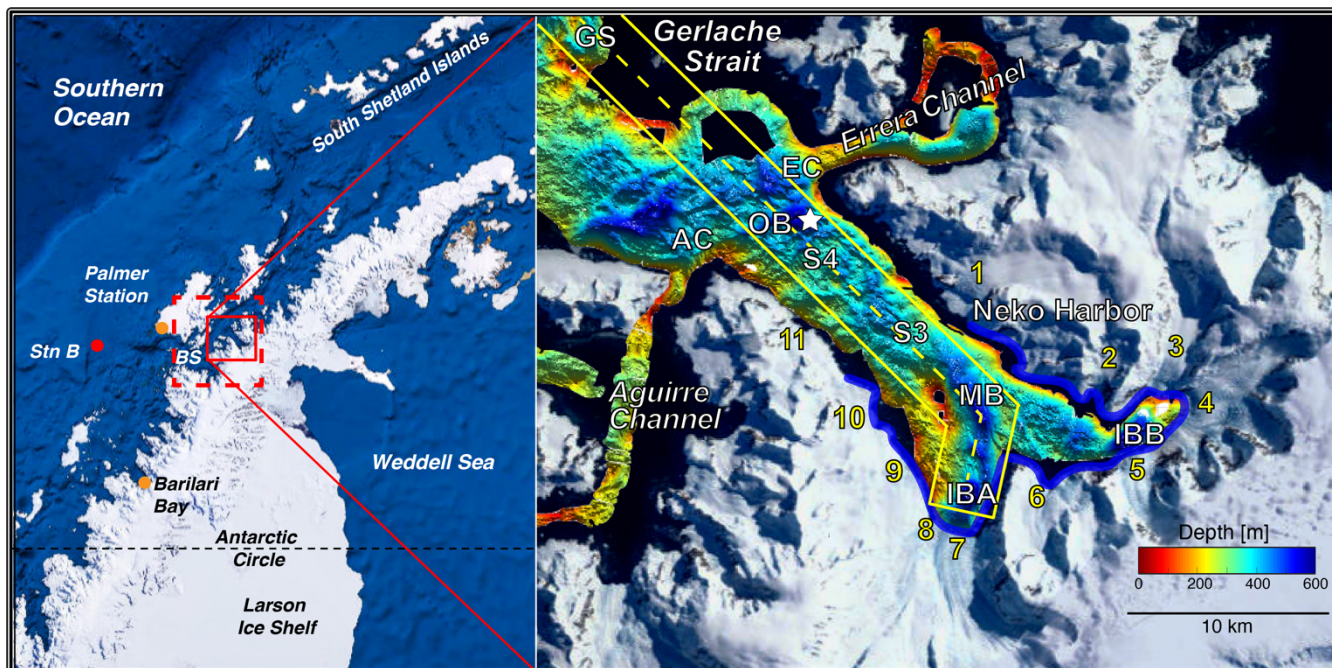
Figure 1. Regional map of study region (red box, inset right) and model domain (dashed red box) with nearby Palmer Station, shelf station (Stn B), and Bismarck Strait (BS). Bathymetric map of Andvord Bay with important stations labeled (GS = Gerlache Strait, AC = Aguirre Channel, EC = Errera Channel, OB = Outer Basin, S4 = Sill 4, S3 = Sill 3, MB = Middle Basin, IBA = Inner Basin A, IBB = Inner Basin B) and the surrounding tidewater glaciers numbered (4 = Moser Glacier, 7 = Bagshawe Glacier). The locations for sediment cores collected in January 2016 and included in this study are indicated by the star. The dashed yellow line indicates the transect along which vertical sections are plotted. Blue outline (inset right) shows glacial fronts where meltwater is introduced in the model.

A total of 18 stations per season were sampled for Fe geochemical variables using acid-cleaned 12 L GO-Flo bottles (General Oceanics) suspended in series on a clean hydroline (Amsteel) and triggered with acid-cleaned Teflon messengers designed by Ken Bruland (UC Santa Cruz). This sampling effort coincided with concurrent CTD stations. Once on board, GO-Flo bottle tops and bottoms were covered with plastic and placed on a wooden rack located within the trace metal clean shipboard plastic "bubble", which was positively-pressurized with HEPA-filtered air. Sample bottles were soaked in a soap detergent overnight with heat applied (60ºC), followed by a one-week soak in 3N HNO_3 (trace metal grade) at room temperature, and finally, a one-week soak in a 3N HCl (trace metal grade) bath at room temperature. Rinsing with ultrapure MilliQ water occurred after each step. Samples for dFe analysis were pressure-filtered (N_2 gas, 99.99%) directly from GO-Flo bottles through 0.2 µm Acropak 200 capsule filters (VWR International), into low-density polyethylene bottles (Nalgene) and acidified to pH 1.7 to 1.8 using HCl (Optima grade, Fisher Scientific). Samples for Fe-binding ligands were similarly filtered in-line but collected in fluorinated high-density polyethylene (Nalgene) bottles, unacidified, and frozen at -20ºC until laboratory analysis back on land. This sampling protocol followed established trace-metal clean methods to the standards of the GEOTRACES program to avoid metal contamination. In addition to the filtered samples, unfiltered seawater was sampled directly from the GO-Flo

bottles and acidified to pH 1.8 and stored for >6 months (up to 2 years) and vacuum-filtered prior to analysis using acid-cleaned 0.4 μm polycarbonate (PC) filters in a Teflon filtration apparatus to determine total dissolvable Fe (TDFe). Labile particulate Fe (LpFe) is calculated as the difference between TDFe and dFe. Particulate samples were collected on 0.4 μm PC filters and stored at -20°C until complete digestion using an HNO_3/HF mixture. The digestion method employed is described in Planquette and Sherrell (2013) and is widely used in the GEOTRACES program (Cutter and Bruland, 2012; Fitzsimmons et al., 2017) .

Attention to cleanliness was applied when sampling icebergs during small boat deployments in the fjord. Floating icebergs were sampled using a clean stainless-steel pickaxe and rust-free stainless-steel screwdriver and plastic mallet for chiseling pieces of ice. Samples were collected by slowly (engine idled) approaching the target piece of floating ice from downwind, limiting the chance of engine exhaust contamination. Each piece of ice was collected above freeboard (sea surface), to reduce the chance the ice was altered by seawater and rinsed with MilliQ prior to placing into acid-cleaned 2 gallon Ziploc polyethylene bags and storing at -4°C until sample processing. Prior to filtration, ice samples were removed from the freezer and left to melt at ambient shipboard temperatures. Once completely melted, a small incision was made on the Ziploc bags using a clean stainless-steel razor and contents poured into the Teflon filtration manifold or directly into sample bottles, thus collecting samples for dissolved, total dissolvable and particulate trace metal fractions. We note that steel-free tools should be used when available, such as titanium tools and ceramic knives, for the cleanest method for sampling of icebergs.

2.2 Trace metal concentrations

Stored acidified filtered seawater samples were analyzed for Fe at Scripps Institution of Oceanography using flow injection with chemiluminescence methods described by Lohan et al. (Lohan, Aguilar-Islas and Bruland, 2006). Dissolved Fe in the samples was oxidized to iron(III) for 1 h with 10 mM Q-H_2O_2 (Suprapur grade), buffered in-line with ammonium acetate to pH ~3.5 and pre-concentrated and matrix removed on a chelating column packed with a resin (Toyopearl® AF-Chelate-650M). Dissolved Fe was eluted from the column using 0.14 M HCl (Optima grade, Fisher Scientific) and the chemiluminescence was recorded by a photomultiplier tube (PMT, Hamamatsu Photonics). The manifold was modified based on Lohan et al. (2006). Standardization of Fe was carried out with a matrix-matched standard curve (0, 0.4, 0.8, 3.2, 10 nmol kg^{-1} added high purity Fe metal ICP spectrometry standard in 2% HNO_3) using 0.34 nM dFe Pacific surface seawater. Standards were treated identically to samples. Accuracy was assessed by repeated measurements of GEOTRACES coastal and Pacific Ocean reference seawater samples. Our measurements of GSC gave Fe = 1.391±0.115 nM (n = 19, over a three-month period, consensus 1.535±0.115 nM). Our measurements of GSP gave Fe = 0.164±0.024 nM (n = 8, over a one-month period, consensus 0.155±0.045 nM). Consensus values are from the most recent July 2019 compilation (geotraces.org). Precision, determined by replicated analyses of an in-house large-volume reference seawater sample within each analytical session, was typically ±5% or better. For the duration of these analyses, the average limit of detection (defined as 3x the standard deviation of the blank) was 0.036 nM dFe (n = 10).

A subset of the seawater samples and all freshwater samples were run for Fe and Mn at Rutgers University using isotope dilution-inductively coupled plasma mass spectrometry (ICP-MS) methods based on Lagerström *et al.* (2013) and similar to those described in Annett *et al.* (2017). Briefly, 10 mL aliquots of seawater samples were extracted using a commercially available automated SeaFAST pico system (Elemental Scientific, Inc.) after online buffering to pH approximately 6.5 using ammonium acetate buffer, achieving a 25-fold pre-concentration after column elution in 0.4 mL 1.6 M ultrapure nitric acid (Optima grade, Fisher Scientific)(Lagerström *et al.*, 2013). Isotope dilution was used to standardize Fe, while Mn was standardized using external matrix-matched standard treated identically to samples. The analysis of the concentrate was performed on an Element 2 sector-field ICP-MS (Thermo Fisher Scientific). Accuracy and precision ($\pm3\%$, 1SD, for Fe and Mn) was assessed by repeated measurements of in-house large-volume reference seawater samples within each analytical session. Blanks averaged 51 pmol kg^{-1} for Fe ($n = 59$; limit of detection, or LOD = 48 pmol kg^{-1}) and 4 pmol kg^{-1} for Mn ($n = 69$; LOD = 4 pmol kg^{-1}) for all analytical runs. A comparison of the seawater analysis methods employed here is shown in Fig. S1. In general, there is good agreement (average 11% and 6% difference late Spring and Fall, respectively) between the chemiluminescence and ICP-MS methods, comparable to the uncertainty of GEOTRACES consensus values from the intercalibration of 13 trace metal laboratories (for Fe, RSD 10%, https://www.geotraces.org/standards-and-reference-materials/). Total dissolvable trace metals and particle digests, including freshwater dissolved metals (i.e., glacial melt), were analyzed using direct-injection ICP-MS methods using external standards and added In as a matrix and instrument drift corrector for the quantification of particulate Fe, Mn, aluminum (Al), and titanium (Ti) concentrations (Annett *et al.*, 2017).

2.3 Sediment cores and diffusive flux

Cores for this study were collected using a 12-barrel Megacore multi-coring device aboard the R/V *Nathaniel B. Palmer* cruise NBP16-01 in January 2016. Multiple barrels were sampled from a single Megacore deployment. See Taylor *et al.* (2020) for a complete account of coring efforts and Komada *et al.* (2016) for a description of the pore water sampling procedures. Porewater dFe and dMn was determined colorimetrically using the ferrozine and formaldoxime techniques, respectively (Armstrong, Lyons and Gaudette, 1979; Burdige and Komada, 2020). For dFe, hydroxylamine-HCl (0.2% v/v final concentration) was added to the samples before analysis, to reduce any dissolved Fe(III) in the samples to Fe(II). For dMn, a hydroxylamine solution was added to an acidified (pH ~1-2) sample, and an EDTA solution was added to remove interference from a colored Fe complex. Porewater oxygen concentrations were measured using a polarographic microelectrode (Brendel and Luther 1995; Luther *et al.* 1998, 2008). A sequential extraction technique (Poulton and Canfield, 2005; Goldberg *et al.*, 2012) was used to determine sediment Fe speciation for the following fractions: Fe$_{ox}$ (highly reactive, poorly crystalline iron oxides), Fe$_{mag}$ (magnetite), Fe$_{prs}$ (Fe in poorly reactive sheet silicates), Fe$_T$ (total sediment Fe), Fe$_{pyr}$ (Fe in pyrite), and finally Fe$_U$ (unreactive pool under all treatments = Fe$_T$ − (Fe$_{ox}$ + Fe$_{mag}$ + Fe$_{prs}$ + Fe$_{pyr}$)). All extracts were analyzed for Fe by flame Atomic Absorption Spectrometry (for details see Burdige and Komada 2020).

In this study, we investigate the potential for efflux of dissolved trace metals as a source to the overlying water column. Using equation 1, we can estimate the approximate sediment diffusive flux (J_{sed}) for dissolved porewater species.

$$J_{sed} = -\phi D_{sed} \frac{dC}{dz} \qquad (1)$$

In this equation, ϕ is the porosity of the sediments, and was found to be 0.9 on average near the sediment surface. Porewater analyses of dissolved Fe and Mn in the Outer Basin (OB) cores reveal high variability in the top-of-core gradient $(\frac{dC}{dz})$ in porewater Fe and Mn (Fig. S2). An average of two cores gives a gradient of 21.9 µM cm^{-1} dissolved Fe and 3.6 µM cm^{-1} dissolved Mn. Assuming a diffusion coefficient for Fe and Mn in free solution for seawater (D_{SW}) at 0°C to be 3.15×10^{-10} m^2 s^{-1} for Fe(II) and 3.02×10^{-10} m^2 s^{-1} for Mn(II), we can then estimate the diffusion coefficient in the sediments (D_{sed}) by the following relationship (van Duren and Middelburg, 2001; Halbach et $al.$, 2019):

$$D_{sed} = \frac{D_{SW}}{1 - 2\ln\phi} \qquad (2)$$

2.4 Iron-binding ligands

A subset of seawater samples was analyzed for dFe-binding ligands using single analytical window methods. The methods applied here are described extensively in Buck et $al.$ (2018). Briefly, natural seawater samples were titrated with dFe (0-35 nM) in order to fully saturate the natural ligands. Following a 2 hour equilibration with the added Fe, a well-characterized ligand (salicylaldoxime, SA) was added to compete with natural dFe-binding ligands. The concentration of SA used in this study to examine ligands was 25.0 µmol L^{-1} ($\alpha_{Fe(SA)_x} = 115$). After at least 15 minutes of equilibration, the Fe(SA)$_x$ electroactive complex was measured using adsorptive cathodic stripping voltammetry (ACSV) on a hanging mercury drop electrode (BioAnalytical Systems, Incorporated). Peak heights were measured using ECDSOFT and sensitivity was optimized in ProMCC (Omanović, Garnier and Pižeta, 2015). A combination of traditional linearization techniques were previously applied to determine the concentrations and strengths of natural ligands within the seawater sample using ProMCC (Omanović, Garnier, and Pižeta 2015). The uncertainty on modeled complexation parameters was optimized using single or multiple ligand fitting. These methods were applied successfully to the GEOTRACES speciation data sets (Buck, Sohst and Sedwick, 2015; Buck et $al.$, 2018).

We calculate the capacity for the free ligand pool to bind Fe at equilibrium (Fitzsimmons et $al.$, 2015), or $\alpha_{FeL'}$, defined as:

$$\alpha_{FeL'} = 1 + ([eL] \times K), \qquad (3)$$

where eL is the difference between the total ligand concentration (L_t) and the dFe concentration, and K is the conditional stability constant.

2.5 Numerical model simulations

Based on Hahn-Woernle et $al.$ (2020), the ocean in the Andvord Bay region is modeled with the primitive-equation, finite-difference Regional Ocean Model System (ROMS, Haidvogel et $al.$, 2008). The grid has a horizontal resolution of ~350 m and a terrain-following vertical coordinate system with 25 depth layers. Due to the changing terrain, the fixed number of layers,

and surface intensified resolution, the maximum thickness for deeper layers is 84.6 m and the minimum thickness for surface layers is 0.5 m (to better resolve e.g. the surface currents). The domain has three open boundaries: the western end of Bismarck Strait, a passage to the continental shelf in the northwest, and along Gerlache Strait to the northeast (Fig. 1). Boundary and initial conditions were derived from CTD and ADCP observations. The model is forced with tidal and meteorological data (from TPXO8 Egbert and Erofeeva 2002 [updated] and RACMO van Wessem *et al.,* 2014, respectively) and run from November 2015 for five months. After one month, the transient effects, based on dynamics and thermodynamics, were found to no longer be present, and the system was consistent. Only the final four sea-ice free months were analyzed (December through March). Processes like melting of icebergs and floating sea ice are not modeled directly, therefore such local freshwater sources are represented in a surface intensified meltwater input applied along the glacial fronts (for further details see Hahn-Woernle *et al.* 2020). These new freshwater sources include also surface runoff and local melt of glacial ice, while precipitation and snowfall are represented in the meteorological forcing. To represent the seasonal cycle of temperature-induced melting the volume flux of inflowing meltwater follows a bell-shaped temporal distribution peaking at the end of January.

We use this model to identify the potential supply pathways and estimate the hydrographic export of three Fe-rich sources in Andvord Bay: surface glacial meltwater, subsurface subglacial plume, and deep water masses located within the inner basin. For this purpose, we designed three model experiments with numerical "dyes" to track potential iron pathways: one, to track the current seasonal input of meltwater from glaciers in Andvord Bay (*surface meltwater dye experiment*) released along the glacial fronts in the inner fjord at 0-50 m depth (Fig. 1); and two additional experiments involving subsurface water masses in front of Bagshawe Glacier in Inner Basin A (IBA, 64° 53' 36'' S, 62° 34' 48'' W) at two different depths (*subsurface* and *deep dye experiments*, respectively). Due to the model geometry, the mean depths the subsurface and deep dyes were released were 107 (94-120 m) and 314 m (290-342 m), respectively. Covering two horizontal grid cells each (with different thickness), the subsurface and deep dyes had initial volumes of 5 x 10^6 and 11.3 x 10^6 m^3, respectively. It follows from the experiment setup that the surface meltwater dye has a continuous source while the total amount of the other two dyes is a constant as long as they do not leave through the open boundaries of the model domain.

3 Results

3.1 Seasonality and hydrography in Andvord Bay

In Andvord Bay (Fig. 1), seasonal changes in phytoplankton biomass were documented, as indicated by the proxy Chlorophyll-a, which shows a 10-fold concentration decrease across all taxonomic classes between the late spring and fall cruises (Pan *et al.*, 2020). Associated with these changes in primary production, depletion of the surface macronutrients nitrate (N) and silicic acid (Si) were observed (Ekern, 2017). Increased Si concentrations, with respect to nitrate, within the inner fjord are driven by dissolution of biogenic silica sediments, or weathering of the bedrock by contact with the 11 marine-terminating glaciers feeding into Andvord Bay since Si-to-N ratio is highly correlated with MWf below the surface layer (Hawkings *et al.*, 2018; Ng *et al.*, 2020). Surface stocks of macronutrients were never exhausted (Fig. 2). The phytoplankton community was

245 dominated by small size classes, with very few large diatoms (Pan *et al.*, 2020). The microplankton class, including large diatoms, was sparingly present in the Fall, however, benthic cameras captured a large sedimentation event of marine aggregates indicative of a large diatom bloom in late-January. The export of biogenic particles from the surface also showed a distinct seasonality indicated by increased Chlorophyll-a pigment content in seafloor surface sediments in Fall (Ziegler *et al.*, 2020), as well as higher respiration rates from chamber incubation experiments in the Fall compared to Spring (data not shown),

250 although no indication of sulfate reduction was observed in sediment box and Kasten cores (2.3 m long), suggesting that oxygen, nitrate, and metal oxides were sufficient to oxidize organic matter within the upper sediments (C. Smith pers. comm.).
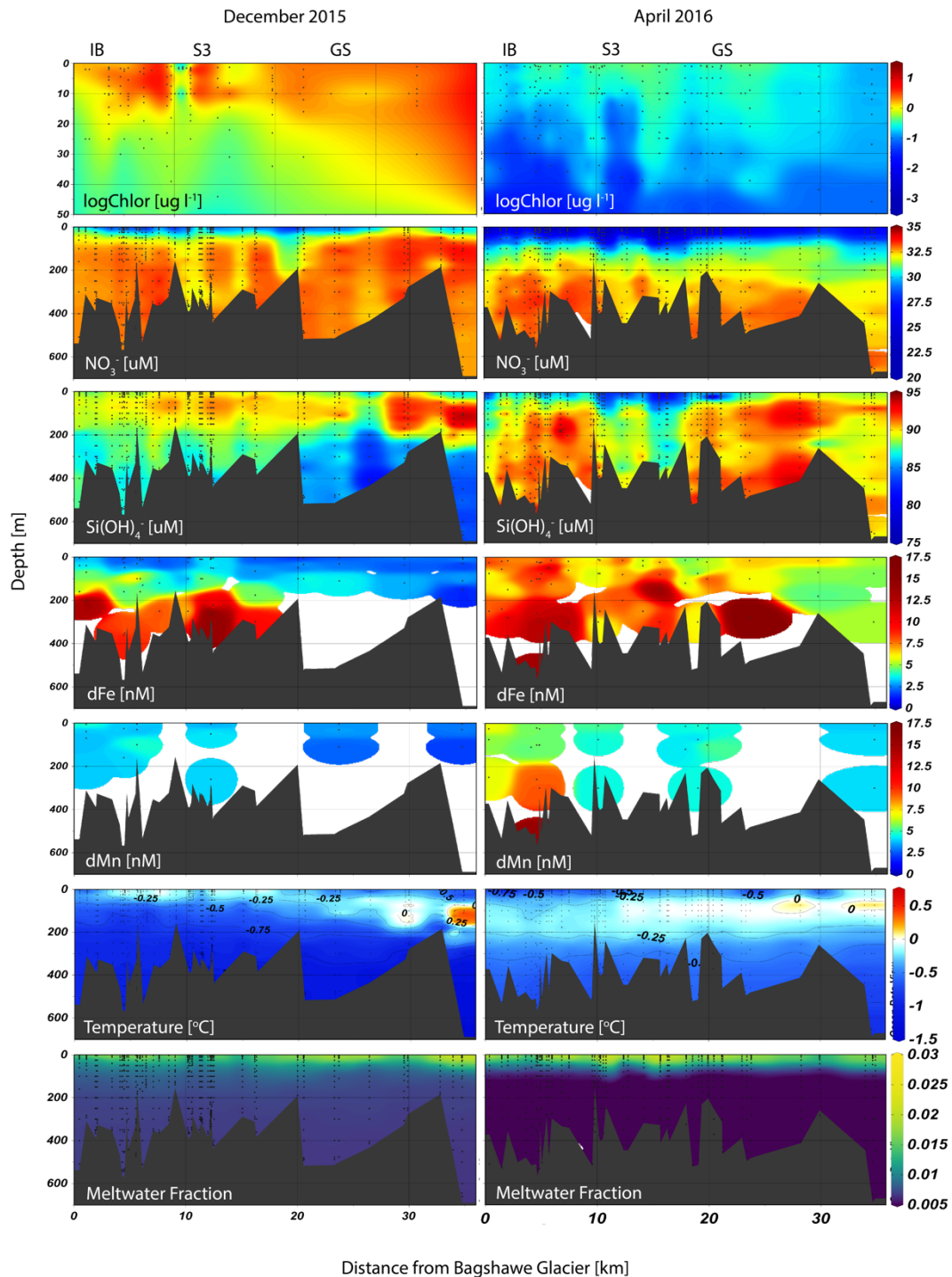
Figure 2. Seasonal phytoplankton, macro-, micronutrient, temperature, and meltwater distributions plotted as sections extending from the inner basin (IB, left) towards Gerlache Strait (GS, right). Plots were made with Ocean Data View visualization software (Schlitzer, 2002, Ocean Data View, last access: 1 February 2021).

255

Derived glacial meltwater fractions (MWf, Fig. 2), based on salinity and oxygen isotopes of seawater, ranged from 0.75-2% in late Spring, and from 0.5-2.5% in the Fall (Pan *et al.*, 2019). The fjord also exhibited a gradient in meltwater content, with highest MWf at the glacier terminus. Using a simple mass balance for the surface layer in Andvord Bay, we estimate an approximate meltwater input of 23600 m^3 d^{-1} in order to account for the observed changes in oxygen isotope ratios. This estimate is within the derived estimates of surface meltwater flux generated by warm atmospheric temperatures (1.4 x 10^4 to 1.2 x 10^5 m^3 d^{-1}; Lundesgaard *et al.*, 2020). The MWf is strongly correlated with phytoplankton abundance within Andvord Bay; for a detailed discussion see Pan *et al.* (2019). We find that glacial meltwater impacts phytoplankton within the fjord, but the geographical influence of meltwater can extend across the shelf, hundreds of kilometers from the coastal inputs (Dierssen *et al.*, 2002; Meredith *et al.*, 2017).

Physical properties measured in the study region showed the dominant water masses in the fjord were Antarctic Surface Water (cold fresh) and Bransfield Strait water (cold salty) (Lundesgaard *et al.*, 2020). However, during late Spring, greater influence of modified Upper Circumpolar Deep Water was observed outside of the fjord, indicated by its distinctly higher temperature at depth, but this water mass is prevented from entering the fjord due to a shallow sill near the fjord mouth in the Gerlache Strait (Fig. 2). Optical measurements recorded a change in the particle concentration and assemblage between the two cruises. Profiles of beam attenuation coefficient and particulate backscattering coefficient showed strong seasonality (see Fig. 4 and discussion in Pan *et al.,* 2019). Pan *et al.* interpreted these optical signatures in the upper water column as a change from a surface biogenic-dominated signal in late Spring to a subsurface lithogenic-dominated signal in the Fall, composed of fine suspended particles contained within plumes. An important feature observed within the fjord was a subsurface neutrally-buoyant plume (~100 m) characterized by a point source of relatively cold and particle-laden water emanating from the terminus of Bagshawe Glacier and extending several kilometers over the inner basin (Fig. S3).

Strong buoyant plumes can drive circulation in fjords via the "meltwater pump", but small amounts of basal and subglacial melt have a negligible effect on circulation in Andvord Bay. While this process is described in-depth for Arctic glaciers, Andvord Bay differs in that ocean temperatures are approximately -1 °C at depth, too cold to ablate the glacier terminus, and neutral buoyancy is reached below the surface layer (indicated by subsurface sediment plumes, Domack and Ishman 1993). However, cold-water glaciers must have some mass loss even at seawater temperatures below the glacial ice melting point. Two important consequences of these plumes are a flux of suspended particulate matter within subsurface "layers" as indicated by high beam attenuation coefficient and optical backscatter (Fig. S3 in Pan *et al.*, 2019), and general mid-water cooling found in the inner fjord (Figure 8 in Lundesgaard *et al.*, 2020). Downstream mixing mechanisms, such as flow over topographic features or wind induced upwelling, can displace plume water closer to the euphotic zone.

3.2 Water column trace metals

Dissolved Fe concentrations in the surface, defined as the upper ~20 m based on similar mixed layer depths (MLD) for both seasons (Lundesgaard *et al.*, 2020), changed seasonally with an overall increase in dFe concentration in the Fall (Fig. 3). The average surface concentration during late Spring was 2.47±0.92 nM (*n* = 21), while in Fall it was 6.67±1.41 nM (*n* = 19).

Water column trace metals are presented in Table S1. These concentrations are within the ranges of dFe determined in prior

290   studies (1-31 nM) in the northern WAP region but indicate that large temporal variability exists in surface waters in this region (Bown *et al.* 2018; Hatta *et al.* 2013; Sanudo-Wilhelmy *et al.* 2002; Ardelan *et al.* 2010; Martin *et al.* 1990). The smaller range of surface concentrations during late Spring suggests that dFe was more tightly controlled by phytoplankton uptake, whereas in the Fall, patchiness among stations arises due to varying proximity to Fe sources and the effects of circulation and mixing. Vertical profiles of dFe showed a steep increase to values greater than 10 nM at the deepest depths sampled during late Spring,

295   especially at stations located within the inner fjord and basins (Fig. 2, 4). In the subsurface (50-150 m), an enriched dFe source was present with average concentrations 3.68 ± 1.52 nM in late Spring and 7.38 ± 2.49 nM in the Fall. Deep water masses greater than 150 m deep had the highest average concentrations of dFe and similar mean concentrations were observed for both seasons (8.79 ± 4.75 nM in late Spring, 6.37 ± 2.38 nM in Fall). The greatest concentrations of dFe were found in the inner fjord and basin stations, with the exception of one station located at the mouth of the fjord near Aguirre Channel (station AC in Fig. 1).

300   Water column concentrations were lower in the Gerlache Strait and fjord mouth. The general shapes of the profiles in late Spring are characteristic of a stratified water column, with dramatic ferriclines below the surface.
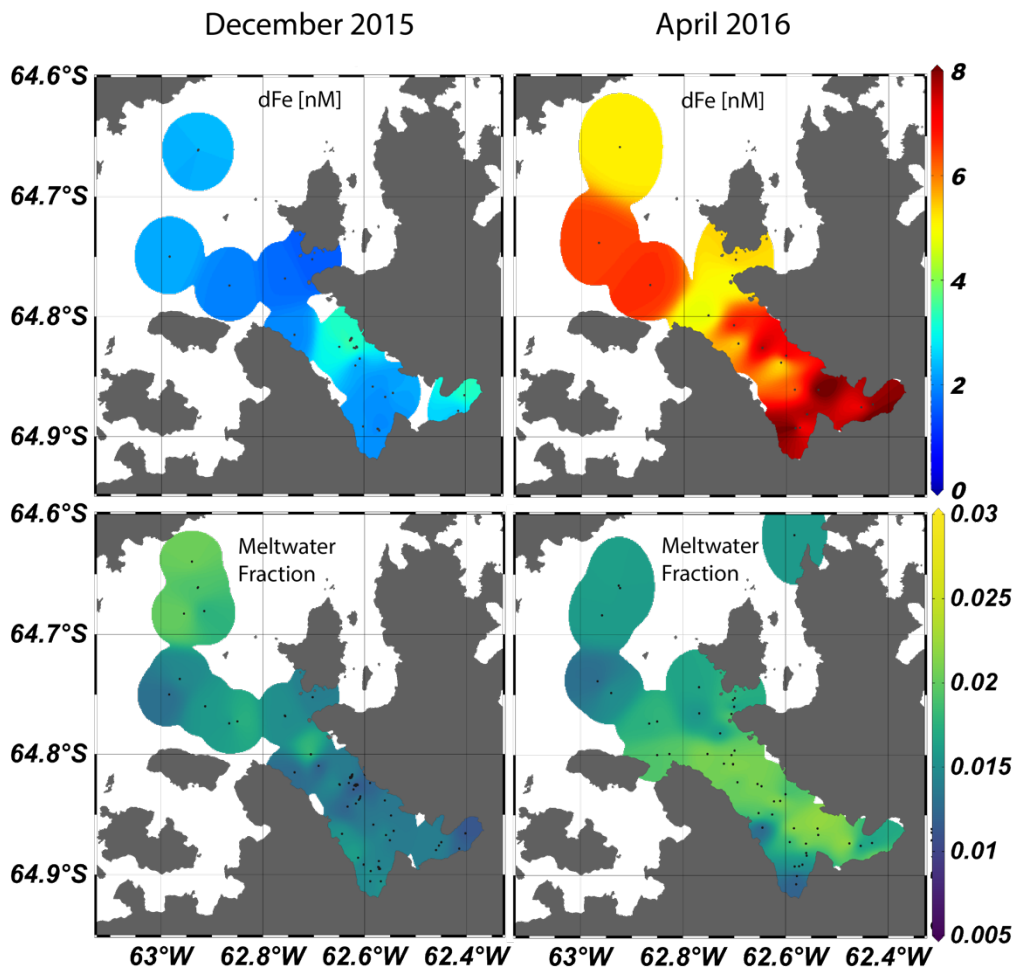
Figure 3. Surface (<20m) dissolved Fe (top) and meltwater fraction (bottom) for late Spring (left two panels) and Fall (right two panels). Plots were made with Ocean Data View visualization software (Schlitzer, 2002, Ocean Data View, last access: 1 February 2021).
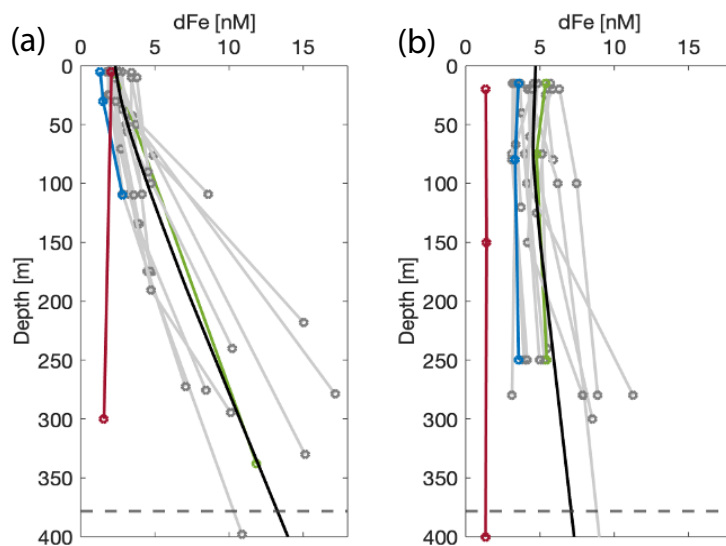
Figure 4. Depth profiles of dissolved Fe [nM] sampled in the Andvord Bay region for December 2015 (A) and April 2016 (B). The colored lines indicate highlighted profiles: the geometric mean of the linearly interpolated data points within Andvord Bay (black), Station B on the continental shelf (red, see Fig. 1), Station GS (Gerlache Strait, blue) and Station S3 (green). Other Andvord Bay stations are shown in grey. The dashed line is the average bottom depth within the fjord.

In the Fall, surface dMn was more than double that observed in the late Spring, but surface dFe showed a greater seasonal increase, such that the dissolved Mn:Fe ratio decreased overall and was more variable than in late Spring. Concentrations of dMn remained below 4.5 nM, even at depth in the late Spring. Labile particulate Mn (LpMn = TDMn – dMn) showed strong co-variation with LpFe and beam attenuation coefficient c(660). The comparatively high surface dissolved Mn:Fe ratios in late Spring were presumably due to intense biological drawdown of Fe during the vernal bloom, evidenced from low concentrations of dFe where phytoplankton biomass (as Chl-a) was highest (Fig. 5a). In the late Spring, dFe is anti-correlated with MWf (Fig. 5c), whereas there was no significant trend between dFe, biomass and MWf variables in the Fall (Fig. 5b,d). The correlation between dMn and dFe was stronger in the Fall, however, compared to the late Spring (Fig. 5e,f).

Labile particulate iron (LpFe = TDFe - dFe) concentrations were elevated in the inner basins in the late Spring and Fall, and strongly correlated with suspended particle concentrations, indicated by optical beam attenuation coefficient c(660) m^{-1} (Fig. 5n). Average TDFe and LpFe concentrations in the surface were comparable to surface waters in Ryder Bay (southern Antarctic Peninsula), where TDFe varied temporally from 57 to 237 nM (Annett *et al.*, 2015). This comparison between LpFe and TDFe is valid since TDFe is much greater than dFe in these two coastal locations, hence it is a good approximation of LpFe. The LpFe maxima were associated with high turbidity in the inner basins, reaching as high as 900 nM at 300 m depth in the Fall (Fig. 6). Dissolved Fe and LpFe were correlated (r^2 = 0.48 late Spring *n* = 19; 0.77 Fall *n* = 28) (Fig. 5g,h). On average, dFe made up 3.1% (late Spring) and 4.6% (Fall) of the total dissolvable pool. The LpMn concentrations displayed similar

seasonality to LpFe and similar association with total particles, but were more strongly correlated in the Fall (Fig. 5l). Dissolved Mn and LpMn were highly correlated ($r^2 = 0.70$ late Spring $n = 19$; 0.79 Fall $n = 28$; Fig. 5i,j). On average, dMn composed 52% (late Spring) and 57% (Fall) of the total dissolvable pool.
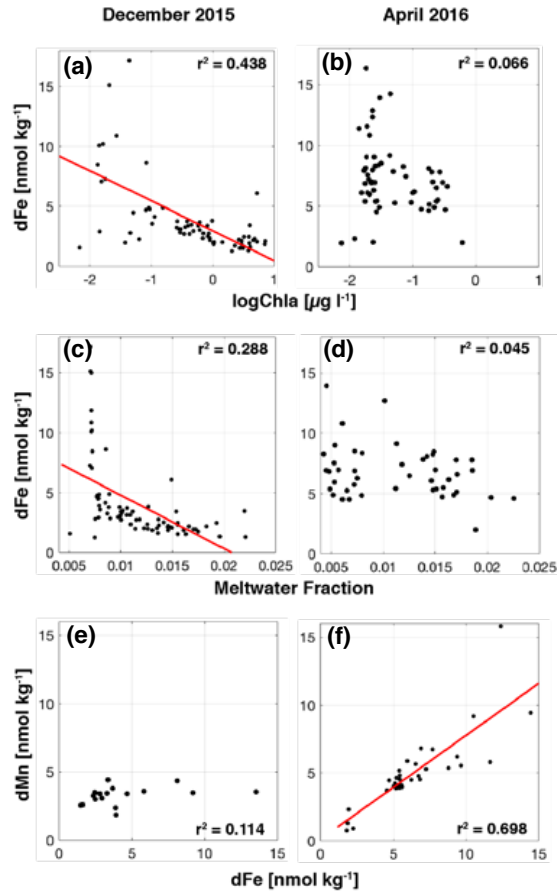
Figure 5. Dissolved trace metals plotted against observed and derived variables for December 2015 (a, c, e) and April 2016 (b, d, f). Dissolved Fe (a-b) versus logChlorophyll-a concentrations. Dissolved Fe (c-d) versus meltwater fraction. Dissolved Mn (e-f) versus dissolved Fe. Least-squares regression lines are shown where they are statistically significant ($p < 0.005$).
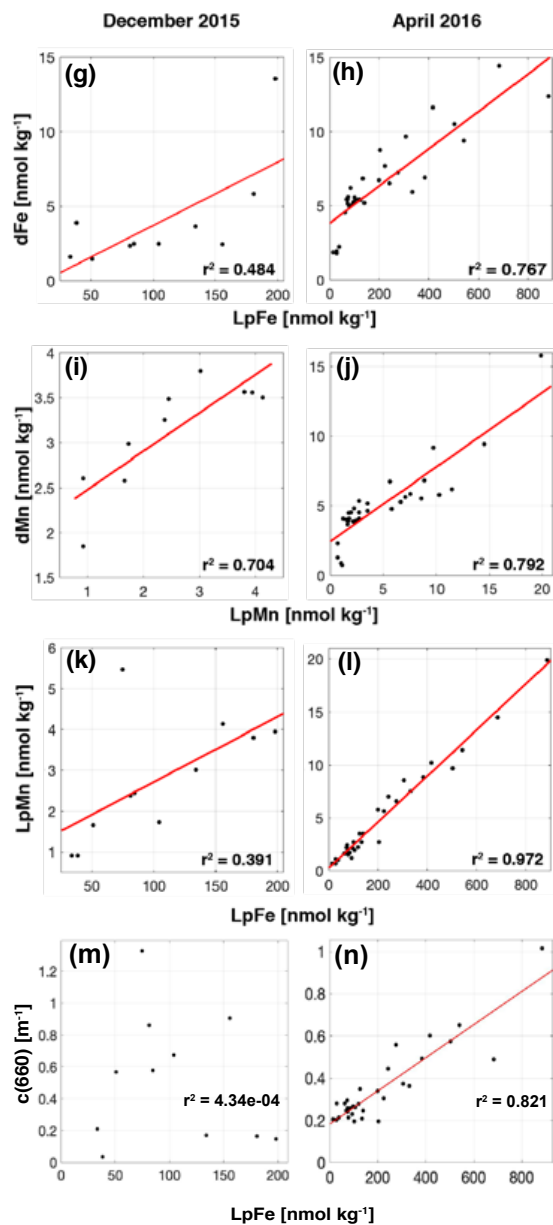
335

Figure 5 (cont'd). Dissolved Fe and Mn concentrations versus labile particulate Fe and Mn for each season. Dissolved Fe (g-h), labile particulate Mn (k-l), and beam attenuation coefficient (m-n) versus labile particulate Fe. Dissolved Mn (i-j) versus labile particulate Mn. Least-squares regression lines are shown where they are statistically significant ($p < 0.005$).
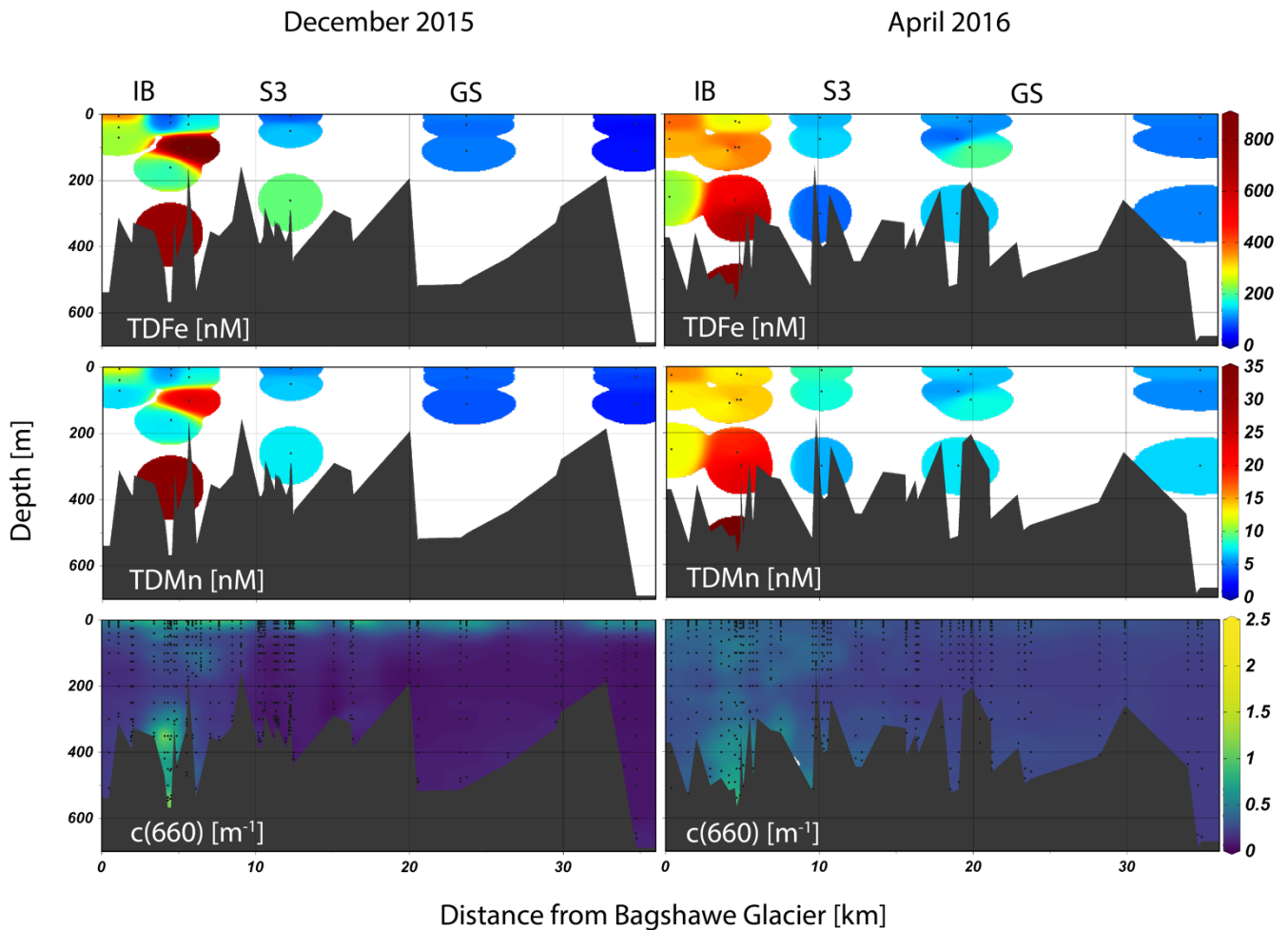
Figure 6. Total dissolvable trace metals and beam attenuation coefficient c(660) for both seasons. The transects are plotted as distance from the Bagshawe Glacier terminus. Plots were made with Ocean Data View visualization software (Schlitzer, 2002, Ocean Data View, last access: 1 February 2021).

3.3 Glacial ice and plume trace metals

Glacial ice and plume samples were analyzed for Fe, Mn, Al, and Ti concentrations, which are presented in Table 1. Three glacial ice samples were analyzed for dFe (72±121 nM) and dMn (49±83 nM). Visual inspection of Glacial Ice 3 and 4 showed these pieces contained low particle loads, while Glacial Ice 1 and 2 had a comparatively high content of dark colored coarse-grained particles. Hence, these and the "clean" glacial ice samples are indicative of the variability of trace metal concentrations in icebergs found in Andvord Bay. Labile particulate trace metal concentrations were two orders of magnitude higher than the dissolved fraction based on two ice samples (41±86 µM LpFe, 3.6±5.1 µM LpMn). We did not determine labile particulate trace metals for Glacial Ice 3 and 4, thus these average labile particulate concentrations are skewed toward a high value. Total

particulate trace metals showed similar concentration variability to the dissolved fraction (95±181 µM TpFe, 2.7±5.1 µM TpMn). For Glacial Ice 3 and 4, the concentration of dMn was greater than TpMn. The ratios of labile and total particulate Mn:Fe were 0.061±0.002 mol:mol and 0.028±0.004 mol:mol, respectively.

355   Dissolved Al and Ti were not analyzed for these ice samples, but total dissolvable and total particulate samples were analyzed for Glacial Ice 1 and 2, and 1-4, respectively. We defined the refractory particulate trace metal concentration as the difference between the total particulate and total dissolvable fractions (RpTM = TpTM - TDTM). Total dissolvable Al and Ti average concentrations were skewed due to the heavy particle load present within Glacial Ice 1 and 2 (603±716 µM TDAl, 20.8±27.1 µM TDTi). Total particulate Al and Ti had similar variability to the total dissolvable fraction and included all four glacial ice

360   samples with averages of 428±790 µM TpAl and 13.4±25.7 µM TpTi, therefore the average total particulate concentrations were lower than the average determined for total dissolvable Al and Ti in Glacial Ice 1 and 2. We found the labile particulate concentration to be a valid comparison to total dissolvable since dFe concentration was on average 1.8±1.5% of TpFe concentration. Thus, the particulate fraction dominated trace metal speciation of total Fe, Mn, Al, and Ti in glacial ice.

Sample Type	Cruise	Location		dFe [nmol kg-1]	TDFe [nmol kg-1]	TpFe [nmol L-1]	dMn [nmol kg-1]	TDMn [nmol kg-1]	TpMn [nmol L-1]	dFe:LpFe	dFe:TpFe	LpMn:LpFe [mol:mol]	TpMn:TpFe [mol:mol]	Description
												(0.017)	(0.017)	Crustal averages
Glacial Ice 1	LMG1510	Inner Basin A		211.59	122228	366332	144.85	7359	10187	0.17%	0.1%	0.059	0.028	floating
Glacial Ice 2	LMG1510	Inner Basin A		n.a.	994	13036	n.a.	61.55	435	n.a.	n.a.	0.062	0.033	floating
Glacial Ice 3	NBP1603	Neko Harbor		1.43	n.a.	56.36	1.62	n.a.	1.41	n.a.	2.5%	n.a.	0.025	floating
Glacial Ice 4	NBP1603	Neko Harbor		1.52	n.a.	52.75	1.81	n.a.	1.26	n.a.	2.9%	n.a.	0.024	floating
			AVG	71.52	61611	94869	49.43	3710	2656	0.17%	1.8%	0.061	0.028	
			STDEV	121.31	69994	181078	82.64	5160	5025		1.5%	0.002	0.004	
Plume 19_100m	NBP1603	Inner Basin A		11.64	419.89	402.26	5.82	15.73	9.169	2.9%	2.9%	0.024	0.023	seawater
Plume 20_100m	NBP1603	Inner Basin A		9.40	538.34	514.90	6.22	17.29	11.73	1.8%	1.8%	0.021	0.023	seawater
Plume 26_110m	NBP1603	Inner Basin A		7.26	227.24	330.37	5.28	11.63	7.665	2.7%	2.2%	0.024	0.023	seawater
Plume 27_110m	NBP1603	Inner Basin A		6.72	202.35	n.a.	4.79	10.36	n.a.	3.4%	n.a.	0.028	n.a.	seawater
			AVG	8.75	346.95	415.84	5.52	13.75	9.52	2.7%	2.3%	0.024	0.023	
			STDEV	2.25	160.40	93.01	0.62	3.29	2.05	0.7%	0.5%	0.003	0.0002	

Sample Type	Cruise	Location		TDAl [nmol kg-1]	TpAl [nmol kg-1]	TDTi [nmol kg-1]	TpTi [nmol kg-1]	TpFe:TpAl [mol:mol]	RpFe:RpAl [mol:mol]	TpFe:TpTi [mol:mol]	LpFe:TDAl [mol:mol]	TDAl:TDTi [mol:mol]	TpAl:TpTi [mol:mol]	Description
								(0.2)	(0.2)	(7)	(0.2)	(35)	(35)	Crustal averages
Glacial Ice 1	LMG1510	Inner Basin A		1109261	1611691	39878	51906	0.23	0.49	7.06	0.11	28	31	floating
Glacial Ice 2	LMG1510	Inner Basin A		97132	100239	1614.4	1709.0	0.13	3.88	7.63	0.01	60	59	floating
Glacial Ice 3	NBP1603	Neko Harbor		n.a.	259.19	n.a.	6.56	0.22	n.a.	8.59	n.a.	n.a.	40	floating
Glacial Ice 4	NBP1603	Neko Harbor		n.a.	262.50	n.a.	6.58	0.20	n.a.	8.02	n.a.	n.a.	40	floating
			AVG	603197	428113	20747	13407	0.19	2.18	7.82	0.06	44	42	
			STDEV	715684	790458	27057	25679	0.04	2.40	0.40	0.07	23	12	
Plume 19_100m	NBP1603	Inner Basin A		887.79	1719.1	14.57	44.45	0.23	-0.01	9.05	0.46	61	39	seawater
Plume 20_100m	NBP1603	Inner Basin A		965.50	2110.5	13.74	56.07	0.24	-0.01	9.18	0.55	70	38	seawater
Plume 26_110m	NBP1603	Inner Basin A		828.98	1373.4	13.85	34.72	0.24	0.11	9.52	0.33	60	40	seawater
Plume 27_110m	NBP1603	Inner Basin A		n.a.	n.a.	n.a.	n.a.	n.a.	n.a.	n.a.	n.a.	n.a.	n.a.	seawater
			AVG	894.09	1734.3	14.06	45.08	0.24	0.03	9.25	0.44	64	39	
			STDEV	68.48	368.79	0.45	10.69	0.01	0.07	0.24	0.11	6	1	

365 **Table 1. Glacial ice and seawater samples analyzed for dissolved, labile, and total particulate trace metals. Crustal averages from Taylor and McClellen (1995): Mn:Fe (0.017 mol:mol), Fe:Al (0.2), and Al:Ti (35).**

Four seawater samples were collected from 100-110 m depth, corresponding to the core of the subsurface turbidity plume within IBA. Average concentrations of dissolved metals were 8.75±2.25 nM dFe and 5.52±0.62 nM dMn. LpFe (351±148 nM)

370 and LpMn (8.23±2.68 nM) were indistinguishable from the total particulate fractions (416±93 nM TpFe, 9.52±2.05 nM TpMn) within measurement error, including filter splitting and sample distribution uncertainties. The average ratio of labile particulate Mn:Fe was 0.024±0.003 mol:mol. Particles collected from the plume had high concentrations of Al and Ti, but with distinctly different lability from that of Mn and Fe. The TDAl was 894±68 nM while TpAl was 1734±369 nM. Similarly, TDTi was 14.1±0.45 nM and TpTi was 45.1±10.7 nM. The total dissolvable Al:Ti ratio was 64±6 mol mol^{-1} and the total particulate

375 Al:Ti ratio was 39±1 mol mol^{-1}. The Al:Ti ratio is elevated above the crustal ratio (35 mol mol^{-1}) in the total dissolvable fraction, suggesting a larger adsorbed fraction for Al than for Ti.

3.4 Glacial sediments

Solid phase Fe speciation of one sediment core from the outer basin station (OB, 64° 46' 46'' S, 62° 43' 57'' W, ~500 m, collected in January 2016), showed an enrichment of authigenic Fe oxides at the surface. Chemical treatments of the sediments
380 with HCl dissolves poorly crystalline Fe oxy(hydr)oxides (ferrihydrite and lepidocrocite), which are found to be 10% of the total particulate Fe of the surface sediments in this location, compared to an average of 2% below 1.5 cm (Fig. S4). In the surficial sediments, a larger portion of the Fe is associated with poorly labile sheet silicates (e.g. structural Fe(III) in clays, 36%), and a comparable fraction is refractory and is not liberated by any of the solution treatments (31%). Other fractions of particulate Fe are associated with more crystalline Fe oxides (goethite, hematite) and the minerals magnetite and pyrite.
385 Porewater analyses were performed on two OB cores using colorimetric methods, revealing high concentrations of dFe and dMn. Below the well-oxygenated layer (upper ~0.5 cm), but within the upper 10 cm, dFe reaches its peak concentration of 80 µM, while maximum dMn is 6 µM. Down-core from the peak, concentrations tend to decrease for both trace metals, but there is considerable variability between 15 and 25 cm, including several deeper local maxima. The average porewater concentration of dFe in the top 2.5 cm is 26 µM (Fig. S2). There is considerable difference in the porewater concentrations of the two OB
390 cores indicating bioturbation of the sediments resulting in large variability on small scales. Points excluded from the oxygen profiles were below the detection limit, while several samples were lost from the porewater profiles, represented as gaps in the vertical traces of dFe and dMn.

3.5 Fe-binding organic ligands

To gain insight into the speciation of dFe within the fjord, we analyzed seawater samples for Fe-binding ligands and to identify
395 comparative strengths of organic Fe complexes (See *Methods*). There is potential to overestimate ligand concentrations using these methods (Gerringa *et al.*, 2021), however, the trends within these data and interpretations are valid. Analysis of the ligands within Andvord Bay shows a down-fjord gradient in both quantity and quality (all ligand data presented in Table 2). In the late Spring, strong ligands ($LogK_{FeL,Fe'}^{cond} \geq 12.0$) were detected in the surface at stations located within the fjord at concentration levels ranging from 4.06±1.74 nM at Inner Basin A (IBA) to 7.27±1.97 nM at Sill 3 (S3), while only weak
400 ligands ($LogK_{FeL,Fe'}^{cond} < 12.0$) were detected in the Gerlache Strait (GS; 5.72±2.21 nM). An excess of strong ligands, relative to dFe, was detected in the inner basins. A gradient in concentration of undersaturated ligands (eL in Table 2) is observed towards the GS, with increasing eL. Within the fjord, weak ligands were detected at Inner Basin B (IBB), closest to Moser Glacier. In the Fall, total ligand concentrations (L$_t$) were elevated everywhere within the fjord, but the surface ligands were somewhat weaker compared to the late Spring. The greatest concentrations of ligands were found closest to the glaciers (range
405 11.18 – 15.42 nM) and in the GS (12.00±2.94 nM). For both seasons, weak ligands were detected in the subsurface, but a

greater concentration in the Fall suggested that these ligands have a local source within the fjord. Compared to other stations in the Fall, we found the plume to contain a small excess of weak ligands (IBA, 110 m). Interestingly, the highest concentration of strong ligands (17.44±1.12 nM) among all sites was in deep water of Station IBA, at 280 m. This is the deepest depth sampled for Fe-binding ligands and the IBA bottom depth was 382 m. We found a down-fjord gradient in ligand strength at the surface, decreasing with distance from the inner basins ($LogK^{cond}_{FeL,Fe'}$ = 11.95 at IBA, 11.03 at GS).

	Station	Depth [m]	dFe [nM]	Fe' [pM]	L_t [nM]	±	logK	±	eL [nM]	L_t:dFe	$log\alpha_{FeL'}$	$R_{Fe'}$
	IBA	6	1.85	0.62	4.06	1.74	12.13	0.69	2.21	2.2	12.5	
	IBA	160	5.84	5.66	8.18	0.57	11.63	0.20	2.34	1.4	12.0	
	IBB	6	3.36	1.19	6.22	0.52	11.99	0.14	2.86	1.9	12.4	
December	MBA	8	2.12	4.70	2.82	0.37	11.58	0.20	0.69	1.3	11.4	
2015	S3	11	3.41	0.79	7.27	1.97	12.05	0.44	3.85	2.1	12.6	
(LMG1510)	S4	7	2.01	2.39	5.00	1.22	11.44	0.33	2.99	2.5	11.9	
	S4	175	4.76	5.95	5.05	1.06	10.90	0.28	0.29	1.1	10.4	
	GS	6	1.53	6.20	2.26	0.33	11.00	0.14	0.73	1.5	10.9	
	OBB	6	2.50	1.16	5.72	2.21	11.82	0.44	3.22	2.3	12.3	
	IBA	25	7.80	1.15	15.42	2.82	11.95	0.26	7.62	2.0	12.8	85%
	IBA	110	6.72	7.18	8.54	0.88	11.69	0.35	1.82	1.3	12.0	
	IBA	280	14.45	1.82	17.44	1.12	12.42	0.37	2.99	1.2	12.8	
	IBA	80	8.51	3.86	17.62	3.57	11.38	0.27	9.11	2.1	12.3	
	IBB	20	6.89	4.16	11.18	1.39	11.58	0.26	4.29	1.6	12.2	249%
April 2016	IBB	75	5.94	3.64	14.03	1.57	11.30	0.13	8.09	2.4	12.2	
(NBP1603)	MBA	20	4.25	18.70	13.32	4.08	10.37	0.25	9.07	3.1	11.3	297%
	S3	15	5.41	15.67	15.33	2.18	11.54	0.14	9.92	3.0	12.5	1883%
	S4	25	6.93	4.63	15.40	3.11	11.20	0.24	8.47	2.2	12.1	94%
	Fjord Mouth	15	4.69	10.05	6.29	1.29	11.43	0.55	1.60	1.3	11.6	
	Fjord Mouth	120	5.37	6.56	7.34	1.87	11.60	0.68	1.97	1.4	11.9	
	GS	15	5.14	6.82	12.00	2.94	11.03	0.32	6.86	2.3	11.9	10%

Table 2. Ligand concentrations and equilibrium constants detected in seawater samples. Fe' is the free (unbound) iron concentration. L_t is the total ligand concentration. logK is the conditional stability constant. eL is the excess ligand concentration (eL = L_t − [dFe]). $log\alpha_{FeL'}$ is the complexation capacity. $R_{Fe'}$ is the ratio of Fe' of reoccupied stations, expressed as a percentage.

We determined the free (uncomplexed) Fe concentration (Fe' in Table 2) within samples analyzed for Fe-binding ligands. In the surface, a greater mean concentration of Fe' was found in the Fall (8.74±6.43 pM, n = 7) compared to the late Spring (2.44±2.18 pM, n = 7). Water below the surface showed similar concentrations for each season (5.8±0.21 pM late Spring, 4.61±2.22 pM Fall). The greatest concentrations of Fe' were observed mid-fjord at the surface (18.7 pM Fe' at MB, 15.67 pM Fe' at S3) in the Fall.

3.6 Dye experiments

To study the transport pathways for dFe, we use numerical passive dyes in the Hahn-Woernle *et al.* (2020) regional model of Andvord Bay (see Fig. 1 in Hahn-Woernle *et al.,* 2020) to track three potential sources of dFe: surface glacial meltwater (0-50 m) from Bagshawe and Moser Glacier termini, neutrally-buoyant subsurface plume (100 m), and deep water located in IBA

425   (300 m; as in *Methods*). Due to numerous inputs and complex biogeochemical processes which result in observed dFe distributions in time and space, we simplify the problem by assuming no removal over the duration of simulated dye experiments. We use this approach to illustrate the multiple transport pathways for dFe supply to the fjord and surrounding ocean from December through March (St-Laurent *et al.*, 2017). The results are presented first for the surface meltwater experiment, followed by two fixed-volume experiments, referred to as subsurface and deep dye experiments.

430   Most of the surface glacial meltwater dye remains in the upper 100 m throughout the model run, and due to its proximity to the surface, it is quickly dispersed over a large region by relatively rapid surface currents. It takes about 10-15 days for the surface meltwater to exit the fjord mouth, where most ends up in the central and northern Gerlache Strait after 120 days (Fig. S5a).

The subsurface dye (100 m) is spread more rapidly than the deep dye (300 m). After 8 days, the subsurface dye reaches the

435   fjord mouth, which is 4 days before the deep dye, implying it has a shorter residence time within the fjord compared to the deep dye. We loosely define residence time as the model timestamp at which a fixed fraction of dye remains within the fjord domain. After 22 days, 25% of the subsurface dye has left the fjord, while it takes the deep dye almost twice as long (43 days). At the end of the 120 days long model run, less than 18% of the subsurface dye and over 30% of the deep dye remain in the fjord domain (Fig. S6a). Looking at the whole model domain in Fig. 1, which includes Andvord Bay and Gerlache Strait, only

440   59% of the subsurface dye and 75% of the deep dye are still present after 120 days. The missing 41% (25%) has mainly left the model domain through the Gerlache Strait to the north, where these waters mix with Bransfield Strait water and subsequently with the southern Antarctic Circumpolar Front waters.

We analyzed the vertical distribution of the subsurface and deep dyes along the fjord mouth and horizontally over different depth layers. Within the first day, the subsurface dye spreads over the depth range of 20 to 125 m and the deep dye over 125

445   to 500 m (>1% of dye per depth layer). The subsurface dye leaves the fjord mainly within the upper 200 m. After 8 days, as the subsurface dye reaches the fjord mouth (Fig. S5b), the maximum concentration is still found close to its release depth at 100-125 m. Over the next few days, surface layer concentrations (<20 m) increase, but the highest concentration is soon found below 125 m (after 2 weeks) (Fig. S6a).

The deep dye remains mainly below 200 m as it passes the fjord mouth (maximum water depth at the fjord mouth is 360 m).

450   After 12 days, as the deep dye reaches the fjord mouth, the maximum concentration is found below 300 m depth. In contrast to the subsurface dye, the deep dye remains longer in the proximity of the fjord mouth and on several occasions, re-enters the fjord leading to a longer residence time within the fjord (Fig. S5c). The majority of the deep dye leaves the fjord at depths below 100 m and along the southwestern coastline. Both dyes, subsurface and deep, have low concentrations in the upper 100

m of the northeastern flank of the fjord mouth. This is due to the inflow of external water from the GS along the northeastern coastline. Throughout the run, the deep dye is confined to the inner basins of the fjord. In all cases, the dyes remain at higher concentrations and for longer periods in the subsurface fjord waters than in the surface layer, which shows faster transport out of the fjord.

4 Discussion

4.1 Iron sources in a heavily glaciated fjord

Due to the proximity to glaciers and influence of ice within Andvord, we hypothesized meltwaters to be an important source of Fe. We focus on quantifying dissolved, total dissolvable and particulate Fe and Mn, as well as total dissolvable and particulate Al and Ti. Ratios of these elements are treated as proxies for contributions of various endmembers. Candidate endmembers include reducing sediments, weathered crustal material, and biogenic particles (Taylor and McLennan 1995; Twining *et al.*, 2004). Where possible, we estimate fluxes of dFe. We begin by examining the relationship between glacial meltwater and dFe.

4.2 Role of surface glacial meltwater

Glacial meltwater at the surface has the potential to be a significant source of Fe to phytoplankton. There exists a weakly negative correlation between derived MWf and dFe at the start of the melt season (late Spring: $r^2 = 0.29$, n = 30; early-Fall: $r^2 = 0.05$, n = 13; Fig. 5c,d). One possible explanation is that increased meltwater at the surface leads to greater stratification and limits upwelling of Fe-rich deep water, with the effect augmented by removal processes, such as biological drawdown and scavenging of dFe onto sinking particles. Indeed, higher rates of primary production are associated with greater fractions of meltwater in Andvord Bay (Pan *et al.*, 2020). While we observe high concentrations of dissolved and particulate trace metals within glacial ice, we note that the icebergs within Andvord were predominantly "clean" ice, with little sediment embedded in the ice, indicated by relatively low dFe and TpFe (for instance, Glacial Ice 3 and 4 in Table 1). Based on Fe:Al ratios in particles and average values for continental crust (Taylor and McLennan 1995), we estimate 87±22% (*n* = 4) of the particulate Fe contained within Andvord icebergs is terrigenous in origin. This is consistent with mechanical weathering of continental crust followed by inclusion of the particles into the ice (freeze-in, Raiswell *et al.*, 2018). Low Fe:Ti and Al:Ti ratios also reflect a continental crust source, but it is worth noting that Glacial Ice 2 had significantly more Mn and Al, relative to continental Fe and Ti. Further, Mn and Al solid speciation suggests there are high concentrations of Mn- and Al-oxides, which may be formed when crustal material is altered (Raiswell *et al.*, 2018). It is also possible that fjord sediments were the source of particulate matter within Glacial Ice 2, which would correspondingly have higher Mn content (and higher Mn:Fe) than what is found in basal ice interacting with the subglacial environment (Hawkings *et al.*, 2020). Continental crust material delivered to the ocean would contain a relatively low Mn content compared to Fe (Fe is 4% w/w in crustal material, while Mn is 0.08% w/w, Rudnick and Gao 2013).

485   Visual inspection suggests that the majority of the ice within Andvord has relatively low concentrations of particles, whereas basal ice, with dark layers of sediment (Glacial Ice 1 in Table 1), will likely skew the average towards high values (Hopwood *et al.*, 2019). A compilation of TDFe in icebergs in Antarctica estimated an average concentration of 24 µM (Hopwood *et al.*, 2019). Our two measurements of LpFe in glacial ice are different (mean for this study is 61±70 µM LpFe, *n* = 2) but are within the range of concentrations determined in the previous study. Thus, we use our mean concentration (Table 1) as indicative of

490   the glacial ice composition in Andvord to compute the following meltwater fluxes. It is important to note that the mean and median values in glacial ice are likely different, with median values closer to Glacial ice 1 and 2 concentrations. Using a range of estimated surface glacial meltwater volume inputs (2.4×10^4 m^3 d^{-1} for this study based on oxygen stable-isotope mass balance; 1.8×10^4 to 1.2×10^5 m^3 d^{-1} Lundesgaard *et al.*, 2020; 1.1×10^6 m^3 d^{-1} Hahn-Woernle *et al.*, 2020 including other freshwater sources that are not precipitation) and assuming the input of meltwater is distributed evenly over the fjord surface

495   layer, we calculate fluxes on the order of 15 to 704 nmol m^{-2} d^{-1} for dFe and 10 to 487 nmol m^{-2} d^{-1} for dMn. Based on modeling work in this paper, it will become evident that meltwater released to Andvord does not stay within the fjord. Additionally, significant metal loss results from scavenging processes, transferring Fe to depth on sinking particle surfaces, rendering it inaccessible for phytoplankton uptake. Still, the availability of excess macronutrients within Andvord Bay (Fig. 2) means that substantial increases in the supply of trace metals from glacial meltwater could stimulate growth in the euphotic zone if light

500   were not limiting (Pan *et al.*, 2020).

4.3 The nature of Fe in subglacial plumes

The inner basins consistently show higher beam attenuation and particle backscattering coefficients than mid-fjord and shelf stations (see Figure 3 in Supplementary Information in Pan *et al.* 2019). These signals are attributed to ultra-fine suspended sediments (<0.8 µm) contained within a buoyant plume. The high particle backscattering coefficient in the surface at all stations

505   in late Spring is due to the high concentrations of biogenic particles associated with the vernal bloom. Inner basins also show local maxima in beam attenuation coefficients at 70-150 m, as well as approaching the benthic boundary layer (Fig. 6). Buoyant turbulent plumes that spread laterally are consistent with the presence of glacial meltwater plumes, or "cold tongues", which originate at the glacier grounding line (described in Domack and Williams 2011), entrain deep water masses, and resuspend sediments (Straneo and Cenedese, 2015). Since ocean temperatures remained below 0°C in Andvord (see Fig. 2), there is little

510   to suggest basal melting of the ice, as is observed further south along the WAP. It appears reasonable on the basis of the evidence given above, that the subsurface plume signature is subglacial in origin.

Total digestion and subsequent analyses of marine particles collected within the plume revealed high concentrations of weathered crustal sediments (82-86% of TpFe, 61-64% of TpMn), and also ingrowth of authigenic particles most likely consisting of precipitated Fe- and Mn-oxide phases (16-18% TpFe, 36-39% TpMn). These results suggest that the origin of

515   plume particles is a chemically-altered crustal source (see *Supplemental Methods*). Labile particulate Fe is 82-100% of TpFe (Table 1). The Fe:Al and Fe:Ti in plume particles (0.24±0.01 mol mol^{-1} and 9.25±0.24 mol mol^{-1}, respectively) were elevated above the average crustal ratios (0.2 mol mol^{-1} Fe:Al, 7 mol mol^{-1} Fe:Ti), which implies these samples are enriched in Fe

relative to both crustal Al and Ti. In agreement with these results, particulate Al:Ti (39 ± 1 mol mol^{-1}) was elevated above crustal ratios (35 mol mol^{-1}), indicating a large oxide fraction is associated with this particulate matter, since the total

520 dissolvable fraction, more enriched in Al than the total particulate fraction, forms when Al is heavily scavenged on to oxy(hydr)oxides at oceanic pH levels (Kryc *et al.*, 2003). This substantiates our claim that most of the Fe found in the plume is weakly adsorbed to particles and recently precipitated, since dilute HCl leaches liberate the most labile forms of Fe, most likely oxy(hydr)oxides (e.g. ferrihydrite) in addition to some Fe from clays. This could include oxides directly precipitated from the anoxic subglacial source, as well as a potential fraction of oxides derived from fjord sediments and porewaters

525 entrained at the grounding line.

Cold-water glaciers are locations where the subglacial environment flows directly into the fjord with minimal mixing with seawater since lower meltwater production cannot induce much turbulence and vertical currents at the glacier face. We find elevated concentrations of dMn (~15 nM, Fig. 2) emanating from the inner fjord, indicative of the reducing conditions beneath Moser and Bagshawe glaciers, consistent with other studies of subglacial environments (Henkel *et al.*, 2018; Zhang *et al.*,

530 2015). Compared to subglacial fluids in contact with bedrock, we report relatively low concentrations of dFe within the plume (8.75 ± 2.25 nM) <1 km away from the glacier terminus. If we assume a MWf of 0.01 for the plume, and assuming a deep fjord seawater concentration of zero, the subglacial meltwater endmember would have a dFe concentration of 875 ± 231 nM, which is higher than the mean value for TDFe measured within the plume (347 ± 160 nM) suggesting settling loss through flocculation is likely occurring even within 1 km of the grounding line. The subglacial endmember dFe estimated here is lower than the

535 range used to parameterize subglacial inputs from ice shelves to the SO (3 – 30 µM in Death *et al.*, 2014). The long residence time and enhanced chemical weathering beneath large glaciers in west Antarctica (PIG, Thwaites Glacier) could result in larger accumulations of dissolved trace metals in subglacial outflow, compared to small glaciers located along the WAP. However, subglacial discharge from large glaciers occurs at some distance from the open continental shelf waters because of the broad floating horizontal ice shelves, which make up about 45% of the Antarctic coastline (Schodlok *et al.*, 2016). Scavenging during

540 advective transport under ice shelves reduces the flux of dFe upwelled into the euphotic zone 10s – 100s km away from the point source of meltwater discharge (Krisch *et al.*, 2021). Our results suggest that assumptions of high export efficiency to the coastal ocean (i.e., using endmember dFe concentrations from glacial runoff and groundwaters as in Death *et al.*, 2014) potentially overestimates dFe supply from anoxic subglacial environments because significant dFe boundary scavenging occurs during lateral transport. It is therefore important, albeit difficult, to parameterize scavenging and removal at the ice-

545 ocean interface as all studies suggest intense removal of dFe on short time and length scales.

4.4 Role of sediments

Analyses of Andvord Bay sediments reveal they are compositionally distinct from temperate fjords consisting of poorly sorted fine silt and clay, many dropstones, suspension deposits and ice-rafted debris (Eidam *et al.*, 2019). Sediment accumulation rates are spatially variable, but a weak along-fjord gradient is present. These deposits suggest sluggish circulation, allowing

550 for the deposition of sediments close to their source, likely through flocculation processes (Cowan and Powell, 1990).

Profiles of beam attenuation coefficient show highest concentration of particles in the inner basins compared to other station locations (see Figure 4 in Pan *et al.,* 2019). There is little evidence for mechanical resuspension through gravity flows (i.e., turbidites) along the steep basin walls, yet such processes could be responsible for the near-bottom elevation in water column particles (Eidam *et al.*, 2019). The presence of elevated particles in the inner basins is accompanied by the greatest concentrations of dissolved and labile particulate Fe and Mn (Fig. 6), demonstrating the potential of resuspended fjord sediments as a source of dissolved trace metals.

Based on the core top porewater profiles, we estimate the sedimentary efflux to be 43.7 µmol m^{-2} d^{-1} for dFe and 7.2 µmol m^{-2} d^{-1} for dMn, due to diffusion alone (Fig. S2). This magnitude of flux was also observed in the shelf sediments in the vicinity of South Georgia Island in the SO (Schlosser *et al.*, 2018). Abundant epibenthic fauna were observed within Andvord Bay, which mix the sediments through bioturbation while consuming labile organic matter. Taylor *et al.* (2020) used ^{234}Th as a proxy to investigate the effect of bioturbation on short timescales and found Andvord Bay sediments possess a high mixing coefficient down to 5 cm (D_b = 36 cm^2 yr^{-1}) consistent with greater deposition and subsequent utilization of organic carbon in the sediments compared to data from the adjacent continental shelf. We believe this accurately reflects the conditions in this fjord: bioturbation by dense aggregations of epibenthic fauna within the basins.

These flux estimates are not surprising when compared to a global compilation of *in situ* measurements of sedimentary efflux of dFe, which is on average ~12 µmol m^{-2} d^{-1} for water masses located on continental margins and with O$_2$ concentrations greater than 63 µmol L^{-1} (Dale *et al.*, 2015). The bottom water oxygen concentration in Andvord Bay always exceeded 230 µmol L^{-1}. The bottom water O$_2$ concentration for OB at the time sediments were cored, was 270 µmol L^{-1}. Abundant epibenthic fauna found within Andvord (Ziegler *et al.* 2017, 2020) would introduce oxygen to the upper few centimeters of the sediments through bioturbation and could decrease the efflux of reduced metals (Severmann *et al.*, 2010). Taylor *et al.* (2020) found Andvord Bay sediments possessed high inventories of ^{210}Pb relative to open shelf and Palmer Deep stations indicating a high mixing coefficient for sediments between 7 and 22 cm depth on timescales of 100 years (Taylor *et al.*, 2020). The effect of this process is mixing of oxide- and organic carbon-rich surficial sediments further down in the core on short- to long-timescales. These dFe flux estimates, together with solid phase speciation results, highlight the importance of rapid oxidation and precipitation occurring at the seawater interface, which effectively retain most Fe as oxy-hydroxides within the sediments (Burdige and Komada, 2020; Laufer-Meiser *et al.*, 2021). The Fe oxides are enriched within the penetration depth of oxygen (~0.5 cm, Fig. S2 inset) and once bioturbated downward, could be a source of dFe following microbial cycling. Multiple local maxima of porewater dFe were observed deeper in the cores. While dissimilatory iron reduction would be a source for Fe, oxidation of Fe with bottom water O$_2$ and Mn(IV) are important sinks and exert a control on the dFe concentration of deep water masses. The deep inner basin water column samples had high dFe concentrations concomitant with high LpFe concentrations (Fig. 2, 6), suggesting some loss of porewater dFe to the water column and rapid formation of authigenic Fe mineral particles. Therefore, the fluxes calculated from porewater profiles are upper limit estimates because they do not account for oxidative losses at the sediment-water interface (e.g., Burdige and Komada 2020). In the Ross Sea, Marsay *et al.* (2014)

estimated spatially variable efflux spanning 0.028-8.2 μmol m^{-2} d^{-1} based on water column dFe profiles, which might better

585   illustrate the net effect of rapid oxidation of reduced Fe, for which large uncertainties remain (Marsay *et al.*, 2014).

Due to weak midwater circulation, low tidal energy, and stratification of the surface, a disconnect between deep water masses enriched in dFe and the surface of Andvord Bay persists during prolonged quiescent periods. For these reasons, we believe most sedimentary-sourced Fe from diffusion and resuspension is restricted to deep water masses and therefore plays a minor role in dFe concentrations within the upper water column. There is potential, however, for resuspension and entrainment of

590   surface sediments where subglacial meltwater discharges at the grounding line. Due to the low inferred volume of discharge and lack of strong tides in Andvord Bay, it is unclear if resuspended sediments contribute to the total particulate mass within the plume.

The Mn:Fe ratio is a useful signature of the source of dissolved and particulate trace metals in Antarctica and has been applied to the PAL LTER data set (Annett *et al.*, 2017). Applying this same framework to our study, we find that water column

595   dissolved trace metals are heavily influenced by surface glacial ice melt and subglacial meltwater, and to a lesser extent, sediment sources within the fjord, irrespective of season, depth, and meteoric water input (Fig. 7). Due to the shorter residence time of dFe relative to dMn (i.e., inorganic oxidation of Mn(II) is 10^7 times slower than Fe(II), Sherrell *et al.*, 2018), we would expect the porewater dissolved Mn:Fe ratio to tend towards higher values once exposed to the seawater oxidative front. We therefore cannot rule out porewaters as a source of dMn to the water column. A similar process occurs within the plume, where

600   the elevated dissolved Mn:Fe (0.65 mol mol^{-1}) relative to labile particulate Mn:Fe (0.024 mol mol^{-1}) shows the effect of rapid conversion of Fe to authigenic mineral particles. Although we do not have comparable measurements for sedimentary labile particulate Mn, based on labile particulate Mn:Fe, we find that the water column labile particulate Mn:Fe ratio is precisely the same ratio as particles found within the subglacial plume, again irrespective of when and where the sample was taken (Fig. 8), suggesting plume particles remain suspended throughout the fjord water column.
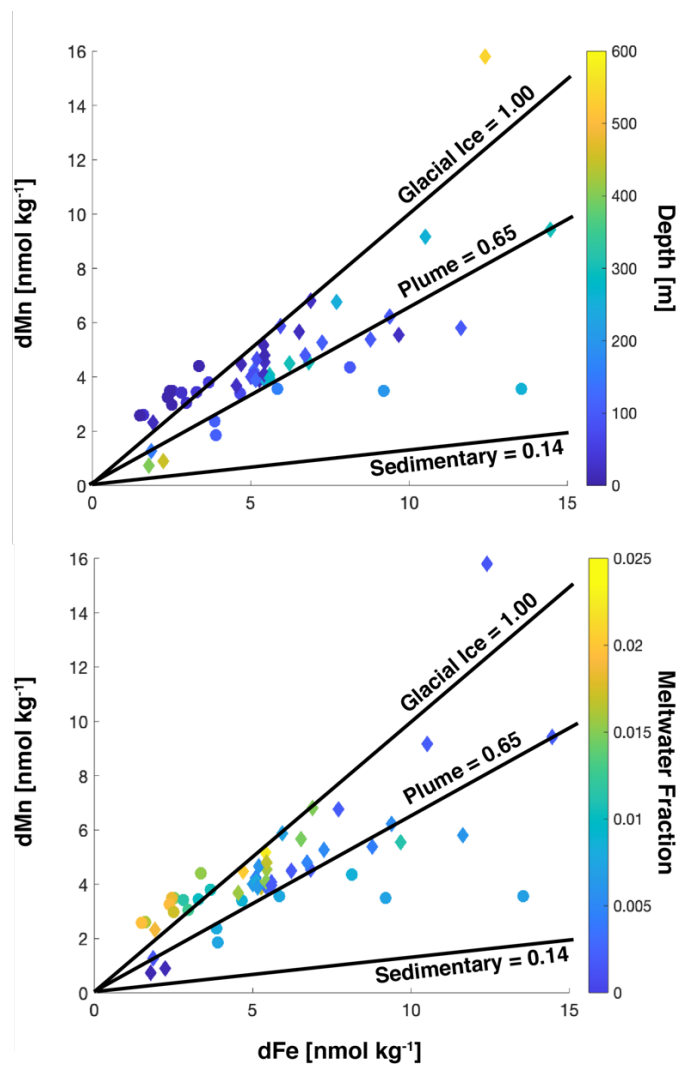
605

Figure 7. Dissolved Fe and Mn plotted for water column samples. The colorbar shows depth (top panel) or meltwater fraction (bottom panel). For both panels, December 2015 cruise is indicated by filled circles and the April 2016 cruise is indicated by filled diamonds. The lines indicate the average Mn:Fe ratio for each candidate source.
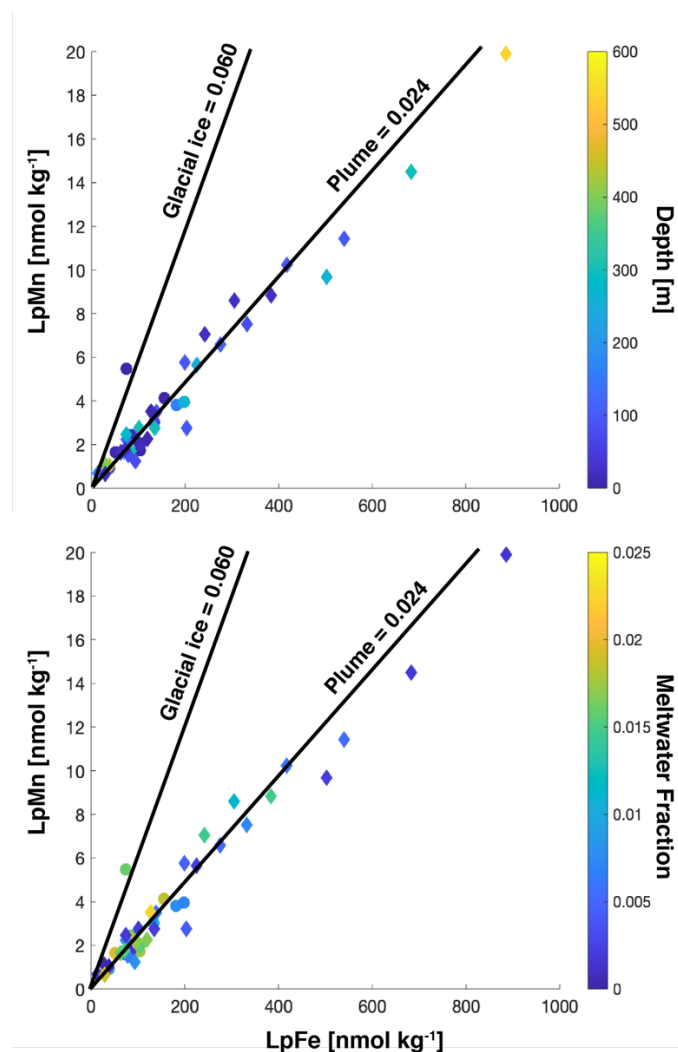
610 **Figure 8. Labile particulate Fe and Mn plotted for water column samples. The colorbar shows the influence of depth (top panel) or meltwater fraction (bottom panel). For both panels, December 2015 cruise is indicated by filled circles and the April 2016 cruise is indicated by filled diamonds. The lines indicate the average ratio of Mn:Fe determined from candidate sources.**

4.5 Organic speciation of dissolved Fe

615 It has been hypothesized that excess ligands (eL = [L$_t$] – [dFe]) increase the solubility of particulate Fe phases (Thuróczy *et al.*, 2011; Gledhill and Buck, 2012; Wagener *et al.*, 2012; Tagliabue *et al.*, 2019). The persistence of exchangeable pools of dFe would therefore be controlled primarily by particle assemblage and organic ligand complements, where pFe dominates total Fe speciation. We observe consistency between late Spring and Fall in the relative contribution of dFe to total Fe (4% to 5% of LpFe, respectively), implying dFe is controlled by scaling closely to LpFe (Fig. 5g,h) since both pools have large

interseason differences. An increase in eL between seasons is observed (average 2.1±1.3 nM late Spring n = 9, 6.0±3.2 nM Fall n = 12). The ligands are likely produced during microbial high-affinity uptake or remineralization processes following the termination of a bloom (Gledhill and Buck, 2012; Hogle *et al.*, 2016). The only subsurface sample to contain strong Fe-binding ligands is the deep inner basin adjacent to Bagshawe Glacier (IBA), possibly indicating these ligands have a sedimentary source. It appears, based on these results, ligands in Andvord Bay have the capacity to complex additional Fe input, as well as prevent significant loss due to scavenging (Thuróczy *et al.*, 2012). The nature of these ligands, taken together with the low concentration of dFe and abundance of LpFe within the plume, leads us to speculate that Fe minerals are the target for ligand-mediated mineral dissolution and perhaps microbial uptake, previously hypothesized to occur in deep-sea hydrothermal vent plumes (Li *et al.*, 2014). In the Fall, despite a greater eL, a lower average conditional stability constant of the ligand pool results in lower complexation capacity and inferred ability to compete with particle binding sites (Ardiningsih *et al.*, 2020). However, the ratio of dFe to LpFe does not reflect a greater enrichment of particles.

While we observe a seasonal increase in the excess ligand concentration, there is no significant change in the ratio of L_t:dFe (late Spring 1.8±0.5, Fall 2.0±0.7). In the Amundsen sector, Thuróczy *et al.* (2012) found waters heavily influenced by the Pine Island Glacier to have L_t:dFe ratios <2.5 throughout the water column, with relatively weaker ligands compared with those found in the highly productive surface waters of the polynya. These findings are similar to an Arctic study, where Ardiningsih *et al.* (2020) detected weaker ligands close to the 79N Glacier terminus along the northeast Greenland shelf compared to the adjacent open ocean. We too identify weaker Fe-binding ligands associated with the glaciers, and only at MB and Sill 3 did we observe elevated L_t:dFe (3.13, and 2.99 respectively, in the Fall). It is possible that sea ice released strong Fe-binding ligands in Andvord that remained in the surface until sampling in the late-Spring (Lannuzel *et al.*, 2015). The presence of excess strong Fe-binding ligands at IBA and S3 during the bloom onset also correspond to elevated NO_3^-:dFe (data not shown) above the threshold for potential Fe-limitation of coastal diatoms in the California Current region (10-12 µmol nmol^{-1} King and Barbeau 2011). The presence of strong Fe-binding ligands might suggest an active microbial strategy in this coastal region to sequester additional Fe from particulate phases during the bloom initiation.

The intense seasonality in primary production and the presence of an undersaturated ligand pool could further increase the bioavailability of particles for downstream communities, where particles within the water column are rare. We calculated the capacity for the free Fe-binding ligands to bind Fe ($\alpha_{FeL'}$ = 1 + (eL • K)). Calculations of $\alpha_{FeL'}$ are included for each sample in Table 2 as well as the inter-seasonal percent change in Fe' for reoccupied stations ($R_{Fe'}$). We find the $\alpha_{FeL'}$ increased between late Spring and Fall at IBA and Sill 4, while a decrease was found at IBB, Sill 3, and Gerlache Strait stations. While all reoccupied stations show an increase in the Fe' concentration ($R_{Fe'}$), the percent change is greatest where $\alpha_{FeL'}$ decreased in the Fall. Thus, the seasonal increase in Fe' reflects the increase in dFe concentrations as well as lower complexation coefficient of weaker Fe-ligand complexes, which contribute most to dFe speciation in the Fall and are associated with surface waters adjacent to glaciers.

These first results of organic speciation of dFe in an Antarctic fjord highlight the importance of seasonal ligand sources in establishing the solubility of new Fe entering the coastal ocean. Accurate ligand pools are not currently represented within SO

biogeochemical models (Death *et al.*, 2014; Oliver *et al.*, 2019; Person *et al.*, 2019; St-Laurent *et al.*, 2019). During the bloom initiation, overall ligand strengths are higher than in the Fall, however, concentrations of ligands increase following the bloom. Concurrently, dFe concentrations increase and do not saturate the ligands to the same extent as in late-Spring. This is due to a greater relative increase in ligand concentrations compared to dFe. Ligand-mediated complexation has the potential to greatly expand the spatial extent over which solubilization of particulate Fe occurs and could be critical for sustaining productivity over a larger geographical region (Lippiatt, Lohan and Bruland, 2010; Ardiningsih *et al.*, 2020). Thus, the size, sinking rate, and composition of particles is critical to their lateral transport and reactivity over time with excess ligands. Our understanding of how cryospheric Fe is transformed after entering the coastal ocean is an important step towards understanding its impact on marine productivity and global biogeochemical cycles of the macronutrients. For the marine Fe cycle, these geochemical transformations control the bioavailability of Fe, while vertical advection and mixing supply this critical micronutrient to the surface ocean and the euphotic zone.

4.6 Using dye experiments to explore Fe sources and export

Rapid communication between the surface and subsurface water masses occurs during katabatic wind events. The large magnitude of vertical shear initializes an upwelling cell close to the inner basins of the fjord. Using an idealized model of a fjord, Lundesgaard *et al.* (2018) found that katabatic winds can laterally export the surface layer, depending on wind velocity, elapsed time of the event, and whether the wind is along-fjord versus off-axis. Within this idealized model of the fjord, the forcing event leads to outcropping of deeper isohalines (up to 0.3 PSU greater) at the surface along the northern flank of the fjord, corresponding to upwelling (see Figure 11 in Lundesgaard *et al.,* 2019). Wind-induced overturning circulation, along with deepening of the mixed layer by up to 25 m, would increase surface dFe concentrations at Sill 3. These general model results showed that wind forcing caused water at depths of 50-150 m to upwell rapidly (within 24 hours) near the glacier termini. This is an important consequence explored further in the highly-resolved model representation of the study region by Hahn-Woernle *et al.* (2020).

The results of the dye experiments allow for the determination of fluxes, either prescribed (in the case of glacial meltwater) or as a result of wind forcing. St. Laurent *et al.* applied similar methods in the Amundsen Sea with explicit coupling of sea ice – ice sheet – ocean interactions (St-Laurent *et al.*, 2017). In a more rigorous biogeochemical model, which included ocean interactions with both sea ice and ice shelves, as well as parameterized Fe reactions, the productive waters in the Amundsen Sea Polynya were supplied by an advected source of dFe from the "meltwater pump" and coastal currents, but this model lacked explicit contributions of subglacial Fe (St-Laurent *et al.*, 2019). These prior modeling results highlight the importance of lateral exchange of surface water masses, providing the impetus to investigate the export of the surface water out of the fjord mouth as explored in the following section.

4.6.1 Surface meltwater Fe sources and export

685 Given that the MWf varied from 1-2.5% within Andvord Bay during the time of sampling, it is expected that the input of glacial meltwater throughout the melt season would supply some dFe to the surface. We extracted vertical profiles of MWf from the model at Sill 3 and Gerlache Strait stations and found that glacial meltwater originating from Bagshawe and Moser glaciers reaches maximum concentration during the summer bloom (late-January 2016), and is relatively constrained to the upper 25 m (Fig. S7b). In early February, when the bloom was terminated, glacial meltwater concentrations in the fjord

690 decreased due to a weakening meltwater input and lateral dispersal. The weakening input is designed to reflect the seasonal cycle of ice melting. Ocean circulation dispersed the meltwater into the Gerlache Strait, as shown by a progressive increase in meltwater in the upper water column throughout the melt season (Fig. S7a). If the volume flux of meltwater input is indeed correlated to the seasonal air temperature cycle, as it is parameterized in the model, the results in Fig. 3 would reaffirm that meltwater is an important control on the accumulation of phytoplankton biomass within Andvord Bay (Pan *et al.*, 2020).

695 The effect of the wind in driving vertical fluxes will vary with wind direction and location within the fjord. The vertical velocity is analyzed for the observation site at Sill 3 and in front of Bagshawe Glacier (IBA). The latter site is an example location for which katabatic winds are expected to lead to intensified upwelling and is also the location of the subsurface and deep dye experiments. Figure 9 (a) and (b) depict the relationship between the katabatic wind events and vertical velocities at 20 m: landward-blowing wind generally leads to downwelling, while seaward-blowing katabatic wind leads to upwelling. Based on

700 observations of dFe from the late Spring prior to a wind event that started on December 11 ([dFe] at 20 m: 1.97 nM at S3, 2.01 nM at IBA), and the modeled maximum vertical velocities during the wind event (2.09×10^{-5} m s^{-1} at S3, 5.08×10^{-5} m s^{-1} at IBA), we computed the upwelling flux of dFe into the surface (20 m) at Sill 3 and IBA to be 3.54 µmol m^{-2} d^{-1} and 8.81 µmol m^{-2} d^{-1}, respectively. These results shed light on the spatial heterogeneity of upwelling conditions within the fjord. Model results for Sill 3 are supported by late Spring observations of elevated dFe and low meltwater fraction at this station (Fig. 3).

705 This is also corroborated by increases in surface dFe concentrations observed during repeat occupations of Sill 3 station before (3.19±1.53 nM dFe) and after the wind event (3.94±1.92 nM dFe). We argue that these punctuated periods of upwelling could be a substantial source of dFe to surface waters in Andvord Bay. Further, this supply, together with the flux of glacial meltwater, provides dFe to fuel phytoplankton community growth.

The efficiency with which wind events export the fjord surface water is explored in the glacial meltwater dye experiment. To

710 account for the changing amount of meltwater in the fjord, export across the fjord mouth in Fig. 9c is given as the percentage of the total amount of dye present within the fjord to resolve the effect of katabatic winds on dispersal dynamics of Fe-rich sources. The meltwater dye experiences up to a 28-fold increased export into the Gerlache Strait during periods of strong along-fjord wind, primarily through the surface. To analyze the correlation between along-fjord wind velocity and the relative meltwater export, we first apply a 24-hr Gaussian filter to the relative export of glacial meltwater (Fig. 9), to exclude tidal

715 signals. Applying the same filter to the wind time series, we find the wind and export data are positively correlated (r = 0.628). The correlation between export and along-fjord winds supports the results by Lundesgaard et al. (2019) who found that

katabatic winds control the export of fjord water. This has important implications for the dispersal of Fe-rich waters downstream, which eventually mix with Fe-poor waters located on the continental shelf (Annett *et al.*, 2017).
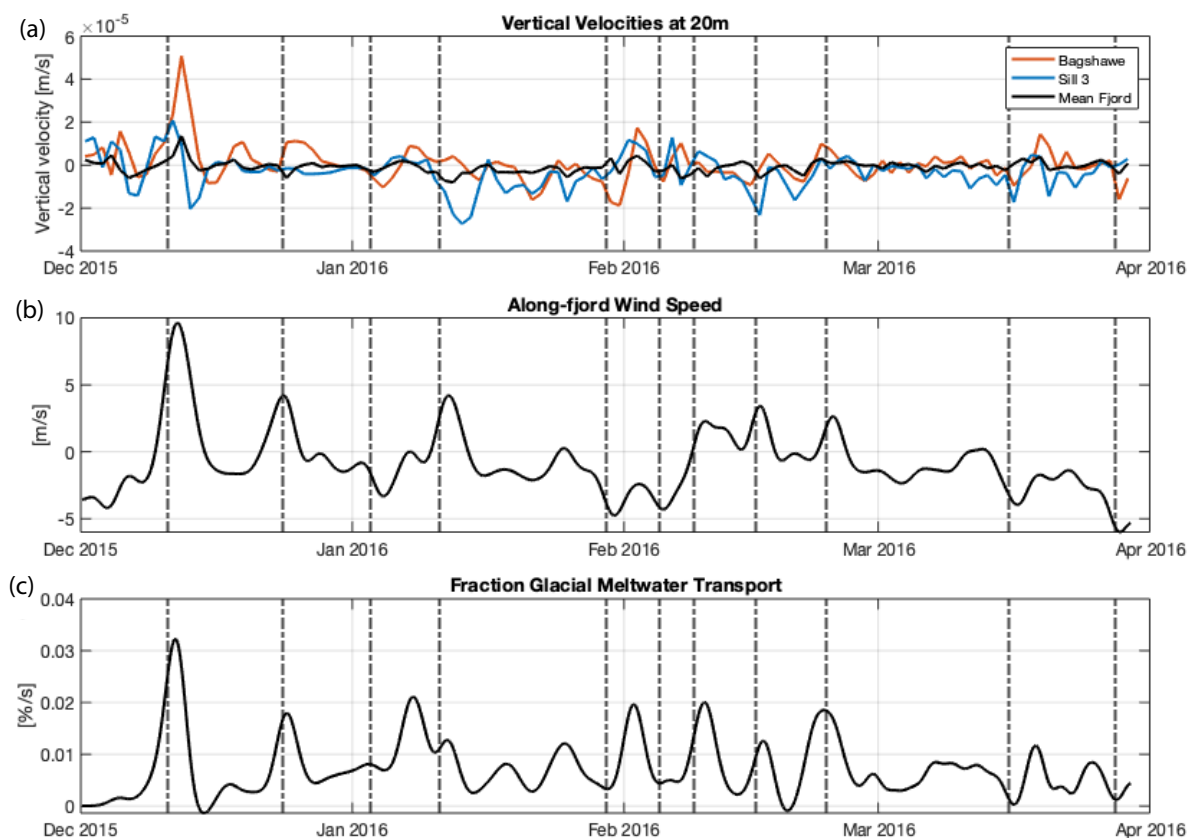
Figure 9. (a) Modeled vertical velocities at 20 m for the following locations: Bagshawe Glacier (IBA), Sill 3 and the fjord region average. 24 hr gaussian filter applied to time series of along-fjord wind velocity (b) and relative meltwater export out of the fjord (c). Wind events exceeding an absolute velocity of 8 m s^{-1} are indicated by vertical dashed lines. Wind speed data is based on bias-corrected RACMO model output for the center of the fjord, used to force the ROMS model. The transport of meltwater dye is shown relative to the total amount of meltwater dye within Andvord Bay to focus on the physical dynamics and not the changes in volume of dye present in the fjord.

4.6.2 Subsurface and deep sources supplying Fe to export

As discussed in the previous section, periods of vertical mixing due to overturning circulation and mixed layer deepening are shown to occur during katabatic wind events (Lundesgaard *et al.*, 2019, 2020). This could be an important mechanism for supplying additional dFe to the fjord surface from the subglacial plume. We examine this possibility here using the subsurface

and deep dye tracers. Prior to the wind event on December 11, the subsurface dye increases gradually in the upper 20 m (Fig. S6b). With the onset of the wind event, the vertical transport of the subsurface dye into the upper 20 m intensifies and reaches a maximum of 32.7 x 10^3 m^3 d^{-1}. In comparison, the deep dye does not enter the upper 20 m prior to the wind event and its maximum vertical transport is only 4.2 x 10^3 m^3 d^{-1}. It follows that katabatic wind events increase mixing in front of Bagshawe
735   Glacier and have a particularly strong effect on water masses at intermediate depth. Assuming a mean concentration of 8.75 nM dFe for the subsurface plume (Table 1) and 8.68 nM dFe for deep (~300 m) IBA waters in the late Spring, these periods of vertical mixing correspond to dFe fluxes of up to 2.81 nmol dFe m^{-2} d^{-1} and 0.36 nmol m^{-2} d^{-1} (3.17 nmol m^{-2} d^{-1} combined) based on the subsurface dye and deep dye, respectively. Following the katabatic wind event, which lasted approximately 11 days, model results show that 36% of the subsurface dye has shoaled above 75 m, with 10% of dye found within the surface
740   layer (<20 m, Fig. S6b). Of the deep water dye, less than 1% is found within the surface layer. The behavior of the deep water masses suggests an insignificant contribution of deep water masses to the surface hydrography and thus, to surface dFe inventory. The vertical fluxes estimated in this section are interpreted as a lower-bound for the contribution of the subsurface plume, since the modeled subglacial plume is a fixed volume, when in reality, subglacial meltwater might be supplied continually throughout the melt season. Compared to the flux of surface glacial meltwater input, and the flux due to subsurface
745   and deep water mixing, the upwelling flux generated by wind events is the largest by an order of magnitude.

The quicker export of the subsurface dye, relative to the deep dye, and therefore the low surface dye concentration, is mainly due to its proximity to the ocean surface (Fig. S5b). The upper water column is controlled by katabatic winds, which exports the surface layer out of the fjord mouth. In contrast, the deep dye is exported more slowly and is more continuously released to Gerlache Strait (Fig. S5c). These modeling results provide evidence for the flushing of fjord water to the Gerlache Strait
750   which coincides with periods of intensified winds. Thus, katabatic winds are important both for replenishing the surface Fe concentrations from the subglacial plume as well as exporting Fe-rich surface waters. It is reasonable to assume that in the absence of a strengthened buoyancy-driven overturning circulation, sources from fjord sediments are negligible in supplying the surface with dFe in Andvord Bay.

4.7 Wind driven meltwater export from WAP fjords

755   Given that the west Antarctic Peninsula hosts the greatest number of glaciomarine fjords on the continent, and multiple katabatic wind events occur throughout the year, wind events can play a crucial role for the export of Fe and Mn to the larger shelf water region. The modeled export of meltwater integrated over the week after the wind event on December 11 is 38x10^7 m^3, which is about 43% of the meltwater input during the same time. For comparison, during the following week, with relatively calm wind conditions, only 20% of the meltwater input is exported. We estimate the Fe export to be 272 mol dFe
760   week^{-1} and 245 mol dMn week^{-1} for this event. However, the warming climate may lessen the likelihood for pulsed export of meltwater-derived Fe by intensifying coastal currents due to declines in sea ice (Moffat *et al.*, 2008), and reduced surface cooling, decreasing the velocity and frequency of katabatic winds over the west Antarctic Ice Sheet (Bintanja *et al.*, 2014).

The large variability in inferred dFe content of glacial meltwaters along the WAP (Annett *et al.*, 2017) means that supply likely depends on fjord-specific processes and future changes in ice volume. Advected sources of dFe remain the largest contribution (~50%) to the inventory on the productive continental shelves (De Jong *et al.*, 2015), while reducing marine sediments are thought to be the main source of dMn (Annett *et al.*, 2015; Sherrell *et al.*, 2015, 2018). Therefore, we believe that a latitudinal assessment of WAP fjords could begin to address variable responses to ocean and atmospheric forcing in these productive ecosystems. Indeed, less than 160 km south of Andvord Bay, observations of warm modified UCDW intrusions and an invigorated "meltwater pump" present an alternative mechanism for sustaining local primary production in Barilari Bay, a glaciomarine fjord (Cape *et al.*, 2019).

The scope of our results should be highlighted. If we assume Andvord Bay is representative of a typical cold-water fjord, and similarly, Barilari Bay is representative of a warm-water fjord (6% MWf at surface, Cape *et al.*, 2019) then we can estimate the glacial meltwater export resulting from a single wind event for the entire western coast of the WAP (see *Supplemental Methods*). A total of 3.6×10^{10} m^3 (36 km^3) of surface glacial meltwater is exported seaward, which corresponds to 2.0×10^6 mol dFe and 1.8×10^6 mol dMn. Thus, katabatic winds are highly efficient at delivering surface meltwater produced near the coast to the continental shelves and ACC, where Fe and Mn limit and co-limit primary production (Browning *et al.*, 2021). However, this volume of surface meltwater exported per year from WAP fjords is small compared to the total basal meltwater production rate due to warm ocean temperatures for the largest ice shelves in Antarctica. Using highly accurate remote sensing topographic measurements Adusumilli *et al.* (2020) found that the major Antarctic ice sheets have a steady-state meltwater production value of 1100 ± 60 km^3 yr^{-1}. In a different modeling study, it was estimated $300 - 800$ km^3 yr^{-1} meltwater enters the SO accounting for observed trends in SO sea surface temperature, sea ice expansion, and sea surface height (Rye *et al.,* 2020). The 'effective' fluxes of Fe and Mn may be lower than what was calculated here because of the non-conservative behavior of these elements during their lateral advection to the shelf. It should be noted that the WAP feeds most directly into the Antarctic Circumpolar Current (ACC), which advects modified coastal waters downstream to the productive Scotia Sea region, potentially magnifying the ecological impact of WAP fjord meltwater production.

5 Conclusion: Andvord Bay as a source of Fe and Mn to shelf waters of the western Antarctic Peninsula

We have argued that, for glaciers terminating in cold-water fjords with a resultant absence of buoyancy-driven upwelling, the interaction of the ice sheet, atmosphere, and surface ocean is important for resupplying the surface waters with Fe throughout the summer season. Using a high-resolution ROMS model of the study region, we showed katabatic wind events result in pulsed export of the surface layer to the adjacent shelf water, while upwelling and vertical mixing entrains subglacial plume water in the inner fjord. Observed surface concentrations of dFe in Fall lend support to these modeled dynamics since elevated concentrations of dFe and meltwater are found within the inner fjord and at Sill 3 (see Fig. 3). At both fjord locations, upwelling of subsurface water masses occurs, potentially entraining subglacial plume water. We summarize the findings of this study in a conceptual diagram showing important seasonal sources of Fe during the growth and melt season (Fig. 10). We highlight

important processes in the diagram using circled number notation. We found ocean temperatures are cold ① and do not melt the fronts of glaciers, but warm summer atmospheric temperatures contribute to the surface melting of glacial ice ②. Variability in dissolved and particulate Fe concentrations in glacial ice imposes large uncertainties in the calculated Fe flux associated with melting. Iron occurs in glacial ice predominantly in the form of refractory Fe-bearing mineral particles ③. Only a small fraction of Fe from these particles may be stabilized by excess organic ligands. Another Fe source is fjord sediments ④, though there is considerable uncertainty shown in the magnitude of this flux because evidence indicates that a significant fraction of porewater Fe rapidly precipitates at the oxidative front, forming a rich surface layer of Fe oxyhydroxides at the sediment surface ⑤. Intense bioturbation of fjord sediments mixes the surface sediments downwards fueling redox processes in deeper sediment layers. The dFe that escapes this sink enriches deep waters within the fjord basins. Small amounts of subglacial meltwater discharge enter the ocean and form turbid buoyant subsurface plumes ⑥. Within the plumes, speciation is dominated by high concentrations of labile authigenic Fe-bearing particles that can be solubilized by Fe-binding organic ligands ⑦. Seaward-blowing katabatic winds ⑧ occur episodically and cause upwelling and vertical mixing supplying additional Fe to the surface phytoplankton assemblage. These intense energetic periods facilitate the dispersion and export of surface Fe, Mn, and meltwater away from the fjord where it is advected downstream in the Gerlache Strait and into the Bransfield Strait ⑨.
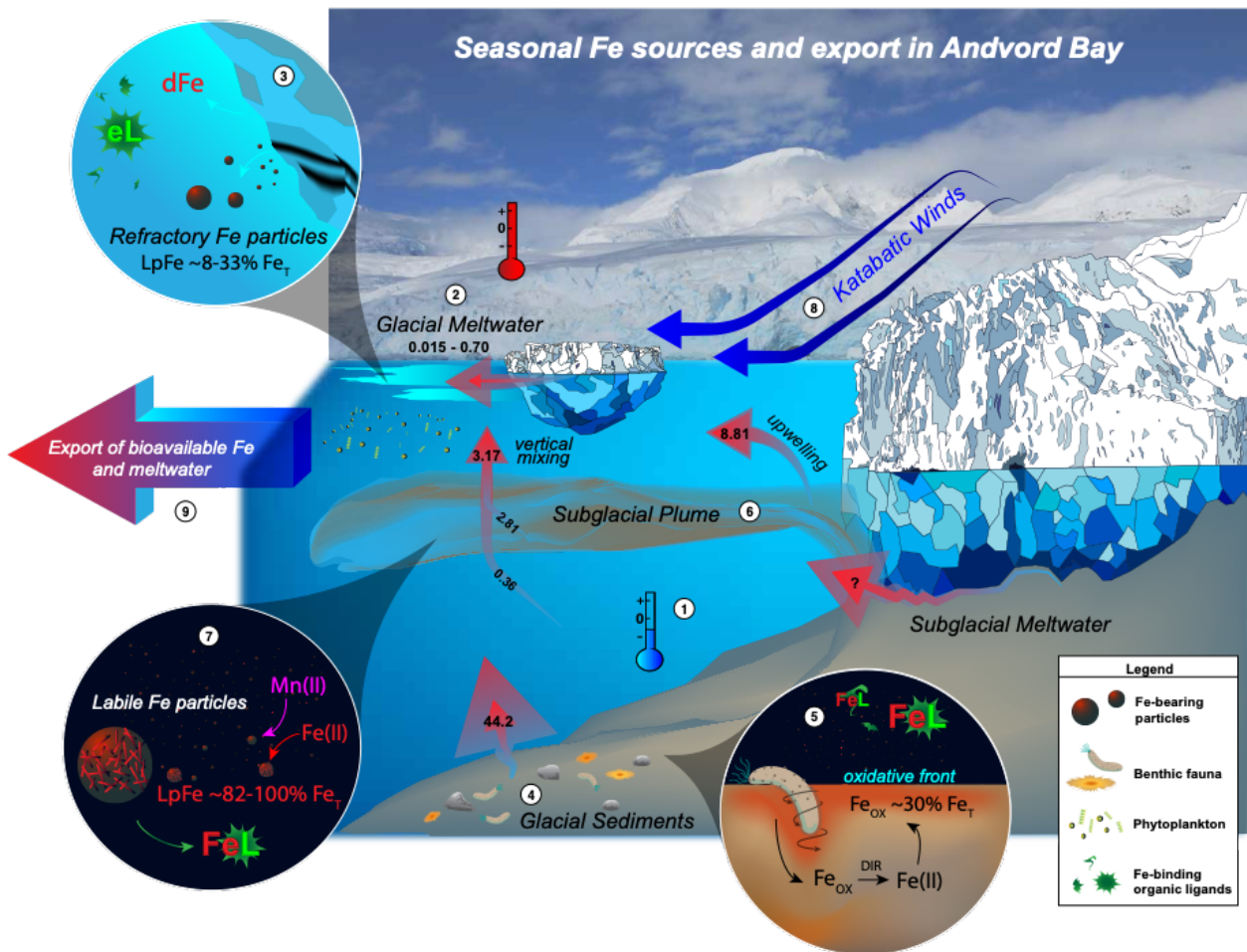
Figure 10. Conceptual diagram showing the important seasonal sources of new Fe during the growth and melt season. The red arrows indicate the major fluxes (in $[\mu M\ m^{-2}\ d^{-1}]$), with the size ranges showing the uncertainty in the measurement – some fluxes are difficult to quantify. These fluxes also vary from season to season and from location to location and may even be going through long-term changes due to human influences, such as climate change, though this is not shown here. The small arrows show internal transformations of Fe, which play an important role in the supply of Fe to phytoplankton. See text for a description of important processes highlighted by circled numbers.

In Andvord Bay, primary production will be sensitive to future changes in subglacial discharge as Antarctic glaciers continue to melt in response to oceanic and atmospheric warming (Smith *et al.*, 2020). In the short term, increased Fe and Mn supply may increase primary production. Conversely, in the long term, increased meltwater discharge will generate a greater flux of sediment to the fjord (Brinkerhoff, Truffer and Aschwanden, 2017), reducing light availability for primary producers, while

stratifying the upper water column and preventing nutrient replenishment (Hopwood *et al.* 2018). A key question outside the scope of this research is how the quantity and quality of Fe-binding ligands will change in the future. To a first approximation, decreases in the magnitude of local phytoplankton blooms and associated ligand sources is expected to reduce efficacy of solubilization of particulate Fe and natural fertilization downstream resulting from this fjord. This climatic trend is not yet realized within Andvord Bay (Eidam *et al.*, 2019), but is expected to decrease dFe export through increased scavenging and sedimentation, further resembling high-Arctic and temperate fjords (Hopwood *et al.*, 2016).

Data availability

All CTD data from this study is available at U.S. Antarctic Program (USAP) Data Center: Vernet, M. et al. (2019) "FjordEco Phytoplankton Ecology Dataset in Andvord Bay" U.S. Antarctic Program (USAP) Data Center. doi: https://doi.org/10.15784/601158.

Author Contributions

K.F. designed the study, conducted the analyses and led the writing of the manuscript. L.H. performed numerical dye simulations. R.M.S., J.R., and K.B. assisted in the preparation of multi-elemental analyses. D.B. provided data for sediment core analyses. L.H., R.M.S., D.B., M.V., and K.A.B. were involved in discussing the results and their implications, and contributed to the drafting of the manuscript.

Competing interests

The authors declare that they have no conflict of interest.

Acknowledgments

The authors would like to thank all participating principal investigators and their affiliates during the NSF FjordEco project (PLR -1443705). Dr. Lauren Manck (University of Montana) assisted with sampling efforts during *NBP1603*. We would like to thank the captain and crew of R/V Laurence M. Gould and RVIB Nathaniel B. Palmer and United States Antarctic Program contractors. We also thank Dr. Brian Powell (University of Hawai`i, Manoa) for helpful comments and for providing resources for the modeling effort. We also would like to thank the two anonymous reviewers for their attention to detail. Their efforts have greatly improved this manuscript.

845 **Financial support**

This research has been supported by the National Science Foundation (grant no. PLR -1443705). Funding for speciation work was funded through an NSF grant (NSF OCE-1558841). K.F. was supported by an NSF GRF (NSF 15-597).

References

Alderkamp, A. C. *et al.* (2012) 'Iron from melting glaciers fuels phytoplankton blooms in the Amundsen Sea (Southern Ocean):
850 Phytoplankton characteristics and productivity', *Deep-Sea Research Part II: Topical Studies in Oceanography*, 71–76, pp. 32–48. doi: 10.1016/j.dsr2.2012.03.005.

Annett, A. L. *et al.* (2015) 'Comparative roles of upwelling and glacial iron sources in Ryder Bay, coastal western Antarctic Peninsula', *Marine Chemistry*. doi: 10.1016/j.marchem.2015.06.017.

Annett, A. L. *et al.* (2017) 'Controls on dissolved and particulate iron distributions in surface waters of the Western Antarctic
855 Peninsula shelf', *Marine Chemistry*. doi: 10.1016/j.marchem.2017.06.004.

Ardiningsih, Indah *et al.* (2020) 'Natural Fe-binding organic ligands in Fram Strait and over the northeast Greenland shelf', *Marine Chemistry*, 224, p. 103815. doi: https://doi.org/10.1016/j.marchem.2020.103815.

Ardiningsih, I *et al.* (2020) 'Sources of Fe-binding organic ligands in surface waters of the western Antarctic Peninsula', *Biogeosciences Discuss.* Copernicus Publications, 2020, pp. 1–25. doi: 10.5194/bg-2020-357.

860 Armstrong, P. B., Lyons, W. B. and Gaudette, H. E. (1979) 'Application of Formaldoxime Colorimetric Method for the Determination of Manganese in the Pore Water of Anoxic Estuarine Sediments', *Estuaries*. Coastal and Estuarine Research Federation, 2(3), pp. 198–201. doi: 10.2307/1351736.

Bintanja, R. *et al.* (2014) 'The future of Antarctica's surface winds simulated by a high-resolution global climate model: 1. Model description and validation', *Journal of Geophysical Research: Atmospheres*. John Wiley & Sons, Ltd, 119(12), pp.
865 7136–7159. doi: 10.1002/2013JD020847.

Bown, J. *et al.* (2018) 'Evidences of strong sources of DFe and DMn in Ryder Bay, Western Antarctic Peninsula', *Philosophical transactions. Series A, Mathematical, physical, and engineering sciences*. The Royal Society Publishing, 376(2122), p. 20170172. doi: 10.1098/rsta.2017.0172.

Boyd, P. W. *et al.* (2019) 'Multi-faceted particle pumps drive carbon sequestration in the ocean', *Nature*, 568(7752), pp. 327–
870 335. doi: 10.1038/s41586-019-1098-2.

Boyle, E. A., Edmond, J. M. and Sholkovitz, E. R. (1977) 'The mechanism of iron removal in estuaries', *Geochimica et Cosmochimica Acta*, 41(9), pp. 1313–1324. doi: http://dx.doi.org/10.1016/0016-7037(77)90075-8.

Brendel, P. J. and Luther, G. W. (1995) 'Development of a Gold Amalgam Voltammetric Microelectrode for the Determination of Dissolved Fe, Mn, O2, and S(-II) in Porewaters of Marine and Freshwater Sediments', *Environmental Science and*
875 *Technology*. doi: 10.1021/es00003a024.

Brinkerhoff, D., Truffer, M. and Aschwanden, A. (2017) 'Sediment transport drives tidewater glacier periodicity', *Nature*

Communications, 8(1), p. 90. doi: 10.1038/s41467-017-00095-5.

Browning, T. J. *et al.* (2021) 'Manganese co-limitation of phytoplankton growth and major nutrient drawdown in the Southern Ocean', *Nature Communications*, 12(1), p. 884. doi: 10.1038/s41467-021-21122-6.

880   Buck, K. N. *et al.* (2018) 'Organic complexation of iron in the eastern tropical South Pacific: Results from US GEOTRACES Eastern Pacific Zonal Transect (GEOTRACES cruise GP16)', *Marine Chemistry*, 201, pp. 229–241. doi: https://doi.org/10.1016/j.marchem.2017.11.007.

Buck, K. N., Sohst, B. and Sedwick, P. N. (2015) 'The organic complexation of dissolved iron along the U.S. GEOTRACES (GA03) North Atlantic Section', *Deep Sea Research Part II: Topical Studies in Oceanography*, 116, pp. 152–165. doi:

885   https://doi.org/10.1016/j.dsr2.2014.11.016.

Burdige, D. J. and Komada, T. (2020) 'Iron redox cycling, sediment resuspension and the role of sediments in low oxygen environments as sources of iron to the water column', *Marine Chemistry*. doi: 10.1016/j.marchem.2020.103793.

Cape, M. R. *et al.* (2019) 'Circumpolar Deep Water Impacts Glacial Meltwater Export and Coastal Biogeochemical Cycling Along the West Antarctic Peninsula ', *Frontiers in Marine Science* , p. 144.

890   Cook, A. J. *et al.* (2016) 'Ocean forcing of glacier retreat in the western Antarctic Peninsula', *Science*, 353(6296), pp. 283 LP – 286. doi: 10.1126/science.aae0017.

Cowan, E. A. and Powell, R. D. (1990) 'Suspended sediment transport and deposition of cyclically interlaminated sediment in a temperate glacial fjord, Alaska, U.S.A.', *Geological Society, London, Special Publications*, 53(1), pp. 75 LP – 89. doi: 10.1144/GSL.SP.1990.053.01.04.

895   Cutter, G. A. and Bruland, K. W. (2012) 'Rapid and noncontaminating sampling system for trace elements in global ocean surveys', *Limnology and Oceanography: Methods*. John Wiley & Sons, Ltd, 10(6), pp. 425–436. doi: https://doi.org/10.4319/lom.2012.10.425.

Dale, A. W. *et al.* (2015) 'A revised global estimate of dissolved iron fluxes from marine sediments', *Global Biogeochemical Cycles*. John Wiley & Sons, Ltd, 29(5), pp. 691–707. doi: 10.1002/2014GB005017.

900   Death, R. *et al.* (2014) 'Antarctic ice sheet fertilises the Southern Ocean', *Biogeosciences*. doi: 10.5194/bg-11-2635-2014.

Dierssen, H. M., Smith, R. C. and Vernet, M. (2002) 'Glacial meltwater dynamics in coastal waters west of the Antarctic peninsula', *Proceedings of the National Academy of Sciences of the United States of America*. doi: 10.1073/pnas.032206999.

Domack, E. W. and Ishman, S. (1993) 'Oceanographic and physiographic controls on modern sedimentation within Antarctic fjords', *Geological Society of American Bulletin*. doi: 10.1130/0016-7606(1993)105<1175:OAPCOM>2.3.CO;2.

905   Domack, E. W. and Williams, C. R. (2011) 'Fine structure and suspended sediment transport in three Antarctic fjords', in. doi: 10.1029/ar050p0071.

van Duren, L. A. and Middelburg, J. J. (2001) 'The benthic boundary layer: Transport processes and biogeochemistry', *Eos, Transactions American Geophysical Union*. doi: 10.1029/01eo00381.

Egbert, G. D. and Erofeeva, S. Y. (2002) 'Efficient Inverse Modeling of Barotropic Ocean Tides', *Journal of Atmospheric and*

910   *Oceanic Technology*, 19(2), pp. 183–204. doi: 10.1175/1520-0426(2002)019<0183:EIMOBO>2.0.CO;2.

Eidam, E. F. *et al.* (2019) 'Variability of Sediment Accumulation Rates in an Antarctic Fjord', *Geophysical Research Letters*. doi: 10.1029/2019GL084499.

Ekern, L. (2017) *Assessing Primary Production via nutrient deficits in Andvord Bay, Antarctica 2015–2016*. University of California, San Diego.

915 Fitzsimmons, J. N. *et al.* (2015) 'The composition of dissolved iron in the dusty surface ocean: An exploration using size-fractionated iron-binding ligands', *Marine Chemistry*. doi: 10.1016/j.marchem.2014.09.002.

Fitzsimmons, J. N. *et al.* (2017) 'Iron persistence in a distal hydrothermal plume supported by dissolved–particulate exchange', *Nature Geoscience*, 10(3), pp. 195–201. doi: 10.1038/ngeo2900.

Gerringa, L. J. A. *et al.* (2015) 'Sources of iron in the Ross Sea polynya in early summer', *Marine Chemistry*.

920 Gerringa, L. J. A. *et al.* (2021) 'Comparing CLE-AdCSV applications using SA and TAC to determine the Fe-binding characteristics of model ligands in seawater', *Biogeosciences*. Copernicus Publications, 18(19), pp. 5265–5289. doi: 10.5194/bg-18-5265-2021.

Gledhill, M. and Buck, K. N. (2012) 'The organic complexation of iron in the marine environment: a review', *Frontiers in microbiology*. Frontiers Research Foundation, 3, p. 69. doi: 10.3389/fmicb.2012.00069.

925 Goldberg, T. *et al.* (2012) 'Controls on Mo isotope fractionations in a Mn-rich anoxic marine sediment, Gullmar Fjord, Sweden', *Chemical Geology*. doi: 10.1016/j.chemgeo.2011.12.020.

Grange, L. J. and Smith, C. R. (2013) 'Megafaunal communities in rapidly warming fjords along the West Antarctic Peninsula: Hotspots of abundance and beta diversity', *PLoS ONE*. doi: 10.1371/journal.pone.0077917.

Hahn-Woernle, L. *et al.* (2020) 'Sensitivity of the summer upper ocean heat content in a Western Antarctic Peninsula fjord', 930 *Progress in Oceanography*, 183, p. 102287. doi: https://doi.org/10.1016/j.pocean.2020.102287.

Haidvogel, D. B. *et al.* (2008) 'Ocean forecasting in terrain-following coordinates: Formulation and skill assessment of the Regional Ocean Modeling System', *Journal of Computational Physics*, 227(7), pp. 3595–3624. doi: https://doi.org/10.1016/j.jcp.2007.06.016.

Halbach, L. *et al.* (2019) 'Tidewater Glaciers and Bedrock Characteristics Control the Phytoplankton Growth Environment in 935 a Fjord in the Arctic', *Frontiers in Marine Science*, p. 254. Available at: https://www.frontiersin.org/article/10.3389/fmars.2019.00254.

Hawkings, J. R. *et al.* (2014) 'Ice sheets as a significant source of highly reactive nanoparticulate iron to the oceans.', *Nature communications*, 5(May), p. 3929. doi: 10.1038/ncomms4929.

Hawkings, J. R. *et al.* (2018) 'The silicon cycle impacted by past ice sheets', *Nature Communications*, 9(1), p. 3210. doi: 940 10.1038/s41467-018-05689-1.

Hawkings, J. R. *et al.* (2020) 'Enhanced trace element mobilization by Earth's ice sheets', *Proceedings of the National Academy of Sciences*, 117(50), pp. 31648 LP – 31659. doi: 10.1073/pnas.2014378117.

Henley, S. F. *et al.* (2020) 'Changing Biogeochemistry of the Southern Ocean and Its Ecosystem Implications ', *Frontiers in Marine Science* , p. 581. Available at: https://www.frontiersin.org/article/10.3389/fmars.2020.00581.

945 Hodson, A. *et al.* (2017) 'Climatically sensitive transfer of iron to maritime Antarctic ecosystems by surface runoff'. The Author(s), 8, p. 14499.

Hogle, S. L. *et al.* (2016) 'Copiotrophic marine bacteria are associated with strong iron-binding ligand production during phytoplankton blooms', *Limnology and Oceanography Letters*. John Wiley & Sons, Ltd, 1(1), pp. 36–43. doi: https://doi.org/10.1002/lol2.10026.

950 Holding, J. M. *et al.* (2019) 'Seasonal and spatial patterns of primary production in a high-latitude fjord affected by Greenland Ice Sheet run-off', *Biogeosciences*. Copernicus Publications, 16(19), pp. 3777–3792. doi: 10.5194/bg-16-3777-2019.

Hopwood, M. J. *et al.* (2015) 'Glacial meltwater from Greenland is not likely to be an important source of Fe to the North Atlantic', *Biogeochemistry*, 124(1), pp. 1–11. doi: 10.1007/s10533-015-0091-6.

Hopwood, M. J. *et al.* (2016) 'Seasonal changes in Fe along a glaciated Greenlandic fjord.   ', *Frontiers in Earth Science*   ,
955 4(March), pp. 1–13. doi: 10.3389/feart.2016.00015.

Hopwood, M. J. *et al.* (2019) 'Highly variable iron content modulates iceberg-ocean fertilisation and potential carbon export', *Nature Communications*, 10(1), p. 5261. doi: 10.1038/s41467-019-13231-0.

Hopwood, M. J. *et al.* (2020) 'Review article: How does glacier discharge affect marine biogeochemistry and primary production in the Arctic?', *The Cryosphere*. Copernicus Publications, 14(4), pp. 1347–1383. doi: 10.5194/tc-14-1347-2020.

960 Hudson, R. J. M., Rue, E. L. and Bruland, K. W. (2003) 'Modeling Complexometric Titrations of Natural Water Samples', *Environmental Science & Technology*. American Chemical Society, 37(8), pp. 1553–1562. doi: 10.1021/es025751a.

Jack Pan, B. *et al.* (2019) 'The optical and biological properties of glacial meltwater in an Antarctic fjord', *PLoS ONE*. doi: 10.1371/journal.pone.0211107.

Jackson, R. H., Straneo, F. and Sutherland, D. A. (2014) 'Externally forced fluctuations in ocean temperature at Greenland
965 glaciers in non-summer months', *Nature Geoscience*, 7(7), pp. 503–508. doi: 10.1038/ngeo2186.

De Jong, J. T. M. *et al.* (2015) 'Sources and fluxes of dissolved iron in the Bellingshausen Sea (West Antarctica): The importance of sea ice, icebergs and the continental margin', *Marine Chemistry*, 177, pp. 518–535. doi: https://doi.org/10.1016/j.marchem.2015.08.004.

Kanna, N. *et al.* (2020) 'Iron Supply by Subglacial Discharge Into a Fjord Near the Front of a Marine-Terminating Glacier in
970 Northwestern Greenland', *Global Biogeochemical Cycles*. John Wiley & Sons, Ltd, 34(10), p. e2020GB006567. doi: https://doi.org/10.1029/2020GB006567.

King, A. L. and Barbeau, K. A. (2011) 'Dissolved iron and macronutrient distributions in the southern California Current System', *Journal of Geophysical Research: Oceans*. John Wiley & Sons, Ltd, 116(C3). doi: 10.1029/2010JC006324.

Krisch, S. *et al.* (2021) 'The 79°N Glacier cavity modulates subglacial iron export to the NE Greenland Shelf', *Nature*
975 *Communications*, 12(1), p. 3030. doi: 10.1038/s41467-021-23093-0.

Kryc, K. A., Murray, R. W. and Murray, D. W. (2003) 'Al-to-oxide and Ti-to-organic linkages in biogenic sediment: relationships to paleo-export production and bulk Al/Ti', *Earth and Planetary Science Letters*, 211(1), pp. 125–141. doi: https://doi.org/10.1016/S0012-821X(03)00136-5.

Lagerström, M. E. *et al.* (2013) 'Automated on-line flow-injection ICP-MS determination of trace metals (Mn, Fe, Co, Ni, Cu and Zn) in open ocean seawater: Application to the GEOTRACES program', *Marine Chemistry*, 155, pp. 71–80. doi: https://doi.org/10.1016/j.marchem.2013.06.001.

Lannuzel, D. *et al.* (2015) 'Organic ligands control the concentrations of dissolved iron in Antarctic sea ice', *Marine Chemistry*, 174, pp. 120–130. doi: https://doi.org/10.1016/j.marchem.2015.05.005.

Laufer-Meiser, K. *et al.* (2021) 'Potentially bioavailable iron produced through benthic cycling in glaciated Arctic fjords of Svalbard', *Nature Communications*, 12(1), p. 1349. doi: 10.1038/s41467-021-21558-w.

Li, M. *et al.* (2014) 'Microbial iron uptake as a mechanism for dispersing iron from deep-sea hydrothermal vents', *Nature Communications*, 5(1), p. 3192. doi: 10.1038/ncomms4192.

Lippiatt, S. M., Lohan, M. C. and Bruland, K. W. (2010) 'The distribution of reactive iron in northern Gulf of Alaska coastal waters', *Marine Chemistry*. doi: 10.1016/j.marchem.2010.04.007.

Lohan, M. C., Aguilar-Islas, A. M. and Bruland, K. W. (2006) 'Direct determination of iron in acidified (pH 1.7) seawater samples by flow injection analysis with catalytic spectrophotometric detection: Application and intercomparison', *Limnology and Oceanography: Methods*. John Wiley & Sons, Ltd, 4(6), pp. 164–171. doi: 10.4319/lom.2006.4.164.

Lundesgaard, Ø. *et al.* (2019) 'Response of an antarctic Peninsula fjord to summer Katabatic wind events', *Journal of Physical Oceanography*. doi: 10.1175/JPO-D-18-0119.1.

Lundesgaard, Ø. *et al.* (2020) 'Hydrography and energetics of a cold subpolar fjord: Andvord Bay, western Antarctic Peninsula', *Progress in Oceanography*. doi: 10.1016/j.pocean.2019.102224.

Luther, G. W. *et al.* (2008) 'Use of voltammetric solid-state (micro)electrodes for studying biogeochemical processes: Laboratory measurements to real time measurements with an in situ electrochemical analyzer (ISEA)', *Marine Chemistry*, 108(3), pp. 221–235. doi: https://doi.org/10.1016/j.marchem.2007.03.002.

Luther III, G. W. *et al.* (1998) 'Simultaneous measurement of O_2, Mn, Fe, I−, and S(—II) in marine pore waters with a solid-state voltammetric microelectrode', *Limnology and Oceanography*. John Wiley & Sons, Ltd, 43(2), pp. 325–333. doi: https://doi.org/10.4319/lo.1998.43.2.0325.

Marsay, C. M. *et al.* (2014) 'Estimating the benthic efflux of dissolved iron on the Ross Sea continental shelf', *Geophysical Research Letters*. doi: 10.1002/2014GL061684.

Meire, L. *et al.* (2017) 'Marine-terminating glaciers sustain high productivity in Greenland fjords', *Global Change Biology*, 23(12), pp. 5344–5357. doi: 10.1111/gcb.13801.

Meredith, M. P. *et al.* (2017) 'Changing distributions of sea ice melt and meteoric water west of the Antarctic Peninsula', *Deep Sea Research Part II: Topical Studies in Oceanography*, 139, pp. 40–57. doi: https://doi.org/10.1016/j.dsr2.2016.04.019.

Mikucki, J. A. *et al.* (2009) 'A Contemporary Microbially Maintained Subglacial Ferrous "Ocean"', *Science*, 324(5925), pp. 397 LP – 400. doi: 10.1126/science.1167350.

Moffat, C. *et al.* (2008) 'A first description of the Antarctic Peninsula Coastal Current', *Deep Sea Research Part II: Topical Studies in Oceanography*, 55(3), pp. 277–293. doi: https://doi.org/10.1016/j.dsr2.2007.10.003.

Mouginot, J. *et al.* (2019) 'Forty-six years of Greenland Ice Sheet mass balance from 1972 to 2018', *Proceedings of the National Academy of Sciences*, 116(19), pp. 9239 LP – 9244. doi: 10.1073/pnas.1904242116.

Ng, H. C. *et al.* (2020) 'Sediment efflux of silicon on the Greenland margin and implications for the marine silicon cycle', *Earth and Planetary Science Letters*, 529, p. 115877. doi: https://doi.org/10.1016/j.epsl.2019.115877.

Oliver, H. *et al.* (2019) 'Modeling Iron and Light Controls on the Summer Phaeocystis antarctica Bloom in the Amundsen Sea Polynya', *Global Biogeochemical Cycles*. John Wiley & Sons, Ltd, 33(5), pp. 570–596. doi: 10.1029/2018GB006168.

Omanović, D., Garnier, C. and Pižeta, I. (2015) 'ProMCC: An all-in-one tool for trace metal complexation studies', *Marine Chemistry*, 173, pp. 25–39. doi: https://doi.org/10.1016/j.marchem.2014.10.011.

Pan, B. J. *et al.* (2020) 'Environmental drivers of phytoplankton taxonomic composition in an Antarctic fjord', *Progress in Oceanography*. doi: 10.1016/j.pocean.2020.102295.

Person, R. *et al.* (2019) 'Sensitivity of ocean biogeochemistry to the iron supply from the Antarctic Ice Sheet explored with a biogeochemical model', *Biogeosciences*. doi: 10.5194/bg-16-3583-2019.

Poulton, S. W. and Canfield, D. E. (2005) 'Development of a sequential extraction procedure for iron: implications for iron partitioning in continentally derived particulates', *Chemical Geology*, 214(3), pp. 209–221. doi: https://doi.org/10.1016/j.chemgeo.2004.09.003.

Pritchard, H. D. and Vaughan, D. G. (2007) 'Widespread acceleration of tidewater glaciers on the Antarctic Peninsula', *Journal of Geophysical Research: Earth Surface*. John Wiley & Sons, Ltd, 112(F3). doi: 10.1029/2006JF000597.

Raiswell, R. *et al.* (2018) 'Iron in Glacial Systems: Speciation, Reactivity, Freezing Behavior, and Alteration During Transport', *Frontiers in Earth Science*. doi: 10.3389/feart.2018.00222.

Raiswell, R. and Canfield, D. E. (2012) 'The Iron Biogeochemical Cycle Past and Present', *Geochemical Perspectives*, pp. 1–220. doi: 10.7185/geochempersp.1.1.

Rignot, E. *et al.* (2013) 'Ice-Shelf Melting Around Antarctica', *Science*, 341(6143), pp. 266 LP – 270. doi: 10.1126/science.1235798.

Rudnick, R. L. and Gao, S. (2013) 'Composition of the Continental Crust', in *Treatise on Geochemistry: Second Edition*. doi: 10.1016/B978-0-08-095975-7.00301-6.

Schlosser, C. *et al.* (2018) 'Mechanisms of dissolved and labile particulate iron supply to shelf waters and phytoplankton blooms off South Georgia, Southern Ocean', *Biogeosciences*. Copernicus Publications, 15(16), pp. 4973–4993. doi: 10.5194/bg-15-4973-2018.

Schodlok, M. P., Menemenlis, D. and Rignot, E. J. (2016) 'Ice shelf basal melt rates around Antarctica from simulations and observations', *Journal of Geophysical Research: Oceans*. doi: 10.1002/2015JC011117.

Schroth, A. W. *et al.* (2014) 'Estuarine removal of glacial iron and implications for iron fluxes to the ocean', *Geophysical Research Letters*, 41(11), pp. 3951–3958. doi: 10.1002/2014GL060199.

Severmann, S. *et al.* (2010) 'The continental shelf benthic iron flux and its isotope composition', *Geochimica et Cosmochimica Acta*, 74(14), pp. 3984–4004. doi: https://doi.org/10.1016/j.gca.2010.04.022.

Sherrell, R. M. *et al.* (2015) 'Dynamics of dissolved iron and other bioactive trace metals (Mn, Ni, Cu, Zn) in the Amundsen Sea Polynya, Antarctica', *Elementa: Science of the Anthropocene*, 3, p. 000071. doi: 10.12952/journal.elementa.000071.

Sherrell, R. M. *et al.* (2018) 'A "shallow bathtub ring" of local sedimentary iron input maintains the Palmer Deep biological hotspot on the West Antarctic Peninsula shelf', *Philosophical Transactions of the Royal Society A: Mathematical, Physical and Engineering Sciences*. doi: 10.1098/rsta.2017.0171.

Smith, B. *et al.* (2020) 'Pervasive ice sheet mass loss reflects competing ocean and atmosphere processes', *Science*, p. eaaz5845. doi: 10.1126/science.aaz5845.

St-Laurent, P. *et al.* (2017) 'Pathways and supply of dissolved iron in the Amundsen Sea (Antarctica)', *Journal of Geophysical Research: Oceans*. John Wiley & Sons, Ltd, 122(9), pp. 7135–7162. doi: 10.1002/2017JC013162.

St-Laurent, P. *et al.* (2019) 'Modeling the Seasonal Cycle of Iron and Carbon Fluxes in the Amundsen Sea Polynya, Antarctica', *Journal of Geophysical Research: Oceans*. doi: 10.1029/2018JC014773.

Straneo, F. and Cenedese, C. (2015) 'The Dynamics of Greenland's Glacial Fjords and Their Role in Climate', *Annual Review of Marine Science*. doi: 10.1146/annurev-marine-010213-135133.

Tagliabue, A. *et al.* (2019) 'The interplay between regeneration and scavenging fluxes drives ocean iron cycling', *Nature Communications*, 10(1), p. 4960. doi: 10.1038/s41467-019-12775-5.

Taylor, R. S., DeMaster, D. J. and Burdige, D. J. (2020) 'Assessing the distribution of labile organic carbon from diverse depositional environments on the West Antarctic Peninsula shelf', *Deep Sea Research Part I: Oceanographic Research Papers*, 156, p. 103166. doi: https://doi.org/10.1016/j.dsr.2019.103166.

Taylor, S. R. and McLennan, S. M. (1995) 'The geochemical evolution of the continental crust', *Reviews of Geophysics*. John Wiley & Sons, Ltd, 33(2), pp. 241–265. doi: 10.1029/95RG00262.

Thuróczy, C.-E. *et al.* (2011) 'Distinct trends in the speciation of iron between the shallow shelf seas and the deep basins of the Arctic Ocean', *Journal of Geophysical Research: Oceans*. John Wiley & Sons, Ltd, 116(C10). doi: 10.1029/2010JC006835.

Thuróczy, C. E. *et al.* (2012) 'Key role of organic complexation of iron in sustaining phytoplankton blooms in the Pine Island and Amundsen Polynyas (Southern Ocean)', *Deep-Sea Research Part II: Topical Studies in Oceanography*. doi: 10.1016/j.dsr2.2012.03.009.

Twining, B. S. *et al.* (2004) 'Cellular iron contents of plankton during the Southern Ocean Iron Experiment (SOFeX)', *Deep-Sea Research Part I: Oceanographic Research Papers*. doi: 10.1016/j.dsr.2004.08.007.

Vernet, M. *et al.* (2008) 'Primary production within the sea-ice zone west of the Antarctic Peninsula: I-Sea ice, summer mixed layer, and irradiance', *Deep-Sea Research Part II: Topical Studies in Oceanography*. doi: 10.1016/j.dsr2.2008.05.021.

Wagener, P., Schwenke, A. and Barcikowski, S. (2012) 'How Citrate Ligands Affect Nanoparticle Adsorption to Microparticle Supports', *Langmuir*. American Chemical Society, 28(14), pp. 6132–6140. doi: 10.1021/la204839m.

van Wessem, J. M. *et al.* (2014) 'Updated cloud physics in a regional atmospheric climate model improves the modelled surface energy balance of Antarctica', *The Cryosphere*. Copernicus Publications, 8(1), pp. 125–135. doi: 10.5194/tc-8-125-

2014.

Wu, J. *et al.* (2001) 'Soluble and colloidal iron in the oligotrophic North Atlantic and North Pacific', *Science*. American Association for the Advancement of Science, 293(5531), pp. 847–849.

Wu, M. *et al.* (2019) 'Manganese and iron deficiency in Southern Ocean Phaeocystis antarctica populations revealed through taxon-specific protein indicators', *Nature Communications*, 10(1), p. 3582. doi: 10.1038/s41467-019-11426-z.

Zhang, R. *et al.* (2015) 'Transport and reaction of iron and iron stable isotopes in glacial meltwaters on Svalbard near Kongsfjorden: From rivers to estuary to ocean', *Earth and Planetary Science Letters*, 424, pp. 201–211.

Ziegler, A. F. *et al.* (2017) 'Glacial dropstones: islands enhancing seafloor species richness of benthic megafauna in West Antarctic Peninsula fjords', *Marine Ecology Progress Series*, 583, pp. 1–14. Available at: https://www.int-res.com/abstracts/meps/v583/p1-14/.

Ziegler, A. F. *et al.* (2020) 'Intense deposition and rapid processing of seafloor phytodetritus in a glaciomarine fjord, Andvord Bay (Antarctica)', *Progress in Oceanography*, 187, p. 102413. doi: https://doi.org/10.1016/j.pocean.2020.102413.